International Journal of Concrete Structures and Materials

RESEARCH

Open Access

High-Performance and Durable Green Geopolymer Based on Slag/Alumina Sludge Ash Incorporating $CuFe_2O_4$ Spinel Nanograins for Enhanced Gamma Radiation Shielding

O. A. Mohamed[1*], Ahmed Hassan[2] and Nesreen R. Abdelwahab[3]

Abstract

This research aims to assess the effectiveness of incorporating thermally treated alumina sludge ash (ASA) as a partial replacement for slag-based geopolymer (SG-Geo) at various ratios (5%, 10%, and 20% by mass) and the integration of cost-efficient $CuFe_2O_4$ spinel nanograins (CF-NGs) at different addition levels (0%, 0.5%, 1%, and 1.5% by weight). The study focuses on enhancing the physico-mechanical features and durability of the geopolymer in aggressive environments, particularly against sulfate (SO_4^{2-}) and chloride (Cl^-) attacks. Key performance indicators include compressive capacity, and non-evaporable water content, to improve the ionizing radiation shielding properties of these eco-friendly geopolymer pastes to advance sustainability objectives. The fabricated samples were tested at 0.662 MeV, 1.17 MeV and 1.33 MeV photon energies as radiation shielding material to achieve sustainability goals. Gamma attenuation parameters (MAC, LAC, MFP, HVL and TVL) were determined experimentally and calculated theoretically using Phy-X/PSD software. The findings indicate that both theoretical and experimental results are consistent, with the radiation protection efficiency improving as ASA content increased up to 20%. The addition of 1.5% CF-NG notably enhanced the compressive strength at 28 days, as well as the gamma attenuation efficiency. Among the various SG-ASA hardened nanocomposites, Mix PS3CF1.5 exhibited superior physical and mechanical properties, along with the most effective gamma radiation shielding performance.

Keywords $CuFe_2O_4$ spinel nanograin, Alumina sludge ash, Slag-based geopolymer, Gamma radiation shielding, Aggressive environments

1 Introduction

Geopolymers, which are made from industrial waste, have gained popularity recently as a promising substitute for cement in a variety of applications, in an attempt to realize the circular economy concept and thus sustainability goals (Chatveera et al., 2024; Yuan et al., 2024; Zhang et al., 2024; Zhao et al., 2023).

It is widely known that, under certain circumstances, any of the pozzolanic substance or material containing reactive SiO_2 and Al_2O_3 that can easily interact with alkali might operate as a precursor for a geopolymer. Calcium aluminum silicate hydrate, or C-A-S-H, is a gel that is created when alkali-activated aluminosilicate materials (AAMs) are made using high-calcium precursors like ground granulated blast-furnace slag, GGBFS (Hamed & Demiröz, 2024). Numerous investigations have demonstrated the adequate mechanical efficiency of the

*Correspondence:
O. A. Mohamed
Ola.abdelaziz.mohamed@psas.bsu.edu.eg
[1] Environmental Science and Industrial Development Department, Faculty of Postgraduate Studies for Advanced Sciences, Beni-Suef University, Beni-Suef 62511, Egypt
[2] Department of Civil Engineering, Beni-Suef University, Beni-Suef, Egypt
[3] Nuclear & Radiological Research Center, Egyptian Atomic Energy Authority, Cairo, Egypt

slag-based geopolymer (Al-Sughayer et al., 2024; Duan et al., 2024; Khoshkbijari et al., 2024; Rashad et al., 2023; Shehata et al., 2022).

Aluminum-containing drinking water treatment sludge (DWTS) as an industrial solid waste poses one of the most critical environmental challenges (Duan et al., 2022a; Mohamed et al., 2022a, 2023a). The conversion of DWT-based sludge into valuable products like supplemental cementitious material (SCM) for use in construction applications has been the subject of numerous studies.

Although there is no set approach for creating geopolymers from WTP-sludges, calcined sludges have produced superior geopolymeric products by increasing the sludge's reactivity and imparting pozzolanic abilities that improve the geopolymeric product (Ferone et al., 2019; Mohamed et al., 2022b; Santosa et al., 2019; Tantawy, 2015). A highly susceptible transition phase is created when alumina sludge is thermally activated between 475 °C and 1100 °C. During this phase, crystalline alumina transforms into amorphous alumina while silica stays in an amorphous form. Within the cement matrix, this phase is probably going to generate calcium silicate hydrates (CSHs) and calcium aluminosilicate hydrates (CASHs) (Duan et al., 2022b; Pham et al., 2021; Shamaki et al., 2021).

To safeguard human life and the natural environment against the dangers of radiation exposure, researchers are searching for various materials that shield against radiation. One of the most important factors that scientists must consider when developing and establishing efficient shielding materials is their capacity to absorb or even attenuate a proportion of ionizing radiation (Mohamed et al., 2022c; Ramadan et al., 2024; Sayed et al., 2024; Selim et al., 2020).

Acceleration devices, healthcare facilities, nuclear power plants, and locations for the disposal of spent fuel often utilize radiation-shielding concrete for safeguarding personnel and property from gamma radiation released by accelerator particle collisions or radioactive sources (Abd Elwahab et al., 2019; Mohsen et al., 2024; Niksarlıoğlu & F. A. kman et al., 2023).

Currently, a lot of researchers are concentrating their efforts on creating novel nano-materials considering their numerous advantages in various disciplines, particularly in the sector of construction and shielding against ionizing radiation (Abd El-Gawad et al., 2023; Hafez et al., 2023; Ibrahim et al., 2023a; Khater & Gharieb, 2024; Mohamed et al., 2023b).

Several academic researchers have recently successfully created a variety of concrete-based ferrite nanoparticles that can absorb gamma radiation, such as $ZnFe_2O_4$, $MgFe_2O_4$, $CoFe_2O_4$, $BaFe_2O_4$, $NiFe_2O_4$, and $CaFe_2O_4$; this is due to their great chemical stability and enormous specific surface area, nano-ferrites have attracted a lot of attention recently owing to their mechanical, optical, electrical, and magnetic capabilities. Consequently, these substances could find use in numerous applications, such as substances for radiation protection (Chinnappa Reddy et al., 2022; Gharieb et al., 2023; Maruthapandian et al., 2016; Ramadan et al., 2020; Reddy et al., 2021; Tobbala, 2019).

Although previous studies have investigated industrial by-products and nanostructured materials for radiation shielding applications, as far as we are aware, no research investigations have been conducted to assess the synergistic effects of incorporating slag /alumina sludge ash as binary precursors with $CuFe_2O_4$ nano grains in gamma radiation shielding applications. Therefore, the innovation of the current work is the design of a green geopolymer based on slag and alumina sludge ash as binary precursors, for gamma radiation shielding in the presence of cost-saving $CuFe_2O_4$ spinel nanograins (CF-NGs). Nanograins of $CuFe_2O_4$ spinel (CF-NG) were fabricated according to the earlier work performed by the authors (Mohamed et al., 2022a). Using both theoretical and experimental approaches, the effect of $CuFe_2O_4$ spinel (CF-NG) nanograins on the behavior of their γ radiation shielding efficiency was assessed. In the current research, the mass attenuation coefficient (MAC) and linear (LAC) attenuation coefficient, MFP, HVL and TVL were calculated experimentally and compared with Phy-X/PSD software results to examine the gamma radiation shielding property of geopolymer paste samples. As well as, the effective atomic numbers (Z_{eff}), effective conductivity (C_{eff}) and effective electron density (N_{eff}) of geopolymer pastes samples were calculating at photon energies ranged from 0.1 MeV to 2.5 MeV.

Environmental contaminants such as salts, alkalis, and acids can cause the structure matrix to expand, the reinforcement to deteriorate, and the composition of hydration products to change, all of which can compromise the structure's long-term durability (He et al., 2024; John et al., 2021).

The substantial influence of sulfate (SO_4^{2-}) and chloride (Cl^-) ions on corrosion processes has been brought to light by recent investigations. In simulated concrete pore solutions, Liu et al. (2024) showed that sulfate ions initiated corrosion at higher thresholds, whereas chloride ions significantly accelerated the corrosion rates of carbon steel. Competitive adsorption onto the steel interface resulted in a reduced corrosion risk when both ions were present together (Liu et al., 2024). Furthermore, Li et al. (2024) created a model to forecast the load capacity of carbon fiber reinforced polymer CFRP-strengthened reinforced concrete (RC) members in a Cl^- environment

and created a diffusion equation for Cl^- anions in CFRP-strengthened RC members (Li et al., 2024). Meanwhile, Luo et al. (2024) developed an important understanding of the life prediction and strength design of reinforced concrete structures in the offshore or subsea regions of subtropical coastal areas by proposing a simplified fatigue simulation and an experimental approach to examine the fatigue efficiency of CFRP-strengthened RC beams under the combined behavior of hot–wet and hot–saline environments and cyclic loads (Luo et al., 2024). In line with our research's focus on the combined impacts of sulfate and chloride ions on material deterioration, these findings highlight the need of taking both ions into account when studying corrosion.

Therefore, the physico-mechanical performance, and durability properties in aggressive environments, particularly against sulfate (SO_4^{2-}) and chloride (Cl^-) attacks were evaluated on the geopolymer pastes made with different ratios of SG-ASA-CF at a sodium silicate/sodium hydroxide (SS/SH) ratio 1.5, as the first investigation into the durability properties of a green geopolymer based on slag and alumina sludge ash in the presence of $CuFe_2O_4$ spinel nanograins.

2 Materials and Methods

2.1 Materials

The slag (SG) was extracted from the Helwan Iron and Steel factory's leftovers, located in Cairo. Following water quenching, this SG took the shape of grains. Blaine surface area and specific gravity of 3400±50 cm^2/ g and 2.86, respectively, were obtained by grinding the slag.

The 105 °C oven-dried water treatment plant sludge (WTPS) was obtained from the Beni-Suef Company for Drinking Water. Using an electrically operated oven set to 500 °C and an ignition rate of 5 °C per 60 s, the dehydrated WTPS was thermally stimulated for 120 min before being cooled gradually.

Table 1 provides information on the chemical content of alumina sludge ash (ASA) and slag (S) analyzed by X-ray fluorescence spectrometry (XRF) using the Xios, stylePW-1400. The information derived from Table 1 demonstrates the significant proportion of silica and alumina in slag and ASA, demonstrating their aluminosilicate composition. X-ray diffraction (XRD) using a Philips Xpert-2000 model was also used to assess the degree of crystallinity in the beginning materials and the composition of the phases of alumina sludge ash and slag. The XRD patterns of SG and ASA are shown in Fig. 1, showing that the silica phase in slag is highly amorphous and that the crystalline phases in ASA comprise albite, quartz, and muscovite.

The alkaline activator was synthesized using NaOH (SH) pellet (>97% purity) and commercial aqueous sodium silicate (Na_2SiO_3; SS) [10.2% Na_2O, 28.9% $SiO_2$and 60.9% H_2O], which were obtained from El Nasr Intermediate Chemicals Company.

Table 1 Chemical compositions of raw materials (% wt)

Oxides	SG	ASA
Al_2O_3	15.90	20.14
SiO_2	33.21	63.45
Fe_2O_3	1.20	5.18
CaO	38.76	4.70
MgO	6.94	1.31
Cl^-	0.18	0.18
SO_3	1.98	0.63
K_2O	0.69	0.64
Na_2O	0.51	0.49
L.O.I	0.63	3.28

The synthesis of $CuFe_2O_4$ spinel nanograins (CF-NG) followed Ref (Mohamed et al., 2022a), the particles size of CF-NG ≈ 7–45 nm with a surface area of 71.63 m^2g^{-1}. As shown in Figures 2, 3, 4, and 5, the physical characteristics of the CF-NG nanograins were examined using a variety of methods, including HR-TEM, N2-adsorption/desorption, XRD, and SEM. In Fig. 4, the characteristic peaks of CF-NG are located at 2θ = 30.1°, 35.5°, 37.1°, 43.1°, 54.7°, 56.95°, and 62.5°, which are consistent with the standard XRD data set of $CuFe_2O_4$ spinel nanograins (JCPDS Card No.034–0425).

2.2 Methods

2.2.1 Synthesis of Geopolymers

Sixteen geopolymer combinations were included in the testing program. Table 2 displays the blend proportions of the geopolymer pastes used in this investigation. To achieve perfect homogeneity, the components of each blend were crushed for one hour in a mechanical ball mill and then being combined in the ceramic ball mill.

As indicated in Table 2, the pastes were made using an SS/SH ratio of 1.5 (3:2) as activator, and a water/binder (w/b) ratio of 0.30 was used for all blends. SG and various series of SG-ASA were individually treated to different ratios of CF-NG (0.5, 1, and 1.5% by weight). The mixing procedure was carried out in compliance with ASTM guidelines (He et al., 2024). Freshly made pastes were put into 25-mm cubic molds and left at room temperature for the entire night, with the relative humidity kept at about 98 ± 2%. This was done to assess the mechanical characteristics. After removing the molds, the cubic samples were submerged in 25 °C normal water till the testing durations (3, 7, 14, and 28 days) were achieved.

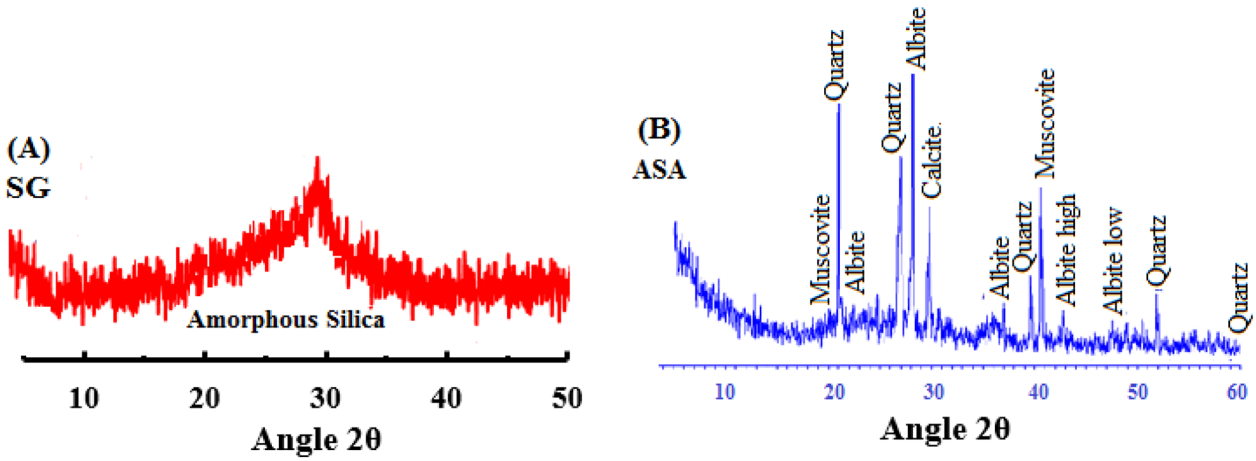

Fig. 1 XRD pattern of the **A** SG, and **B** ASA

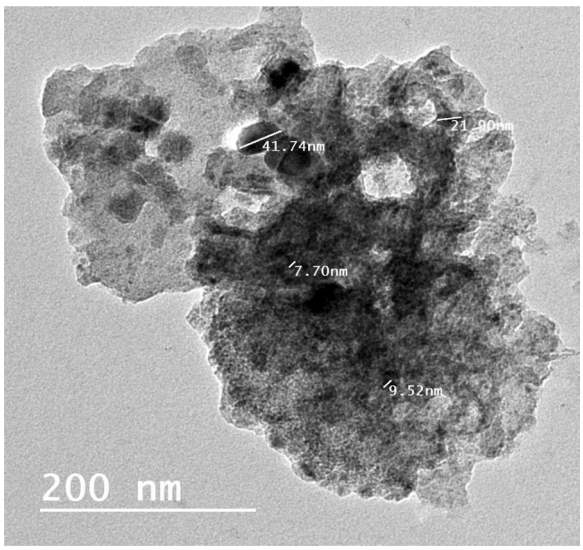

Fig. 2 HR-TEM of CF-NGs nanograins

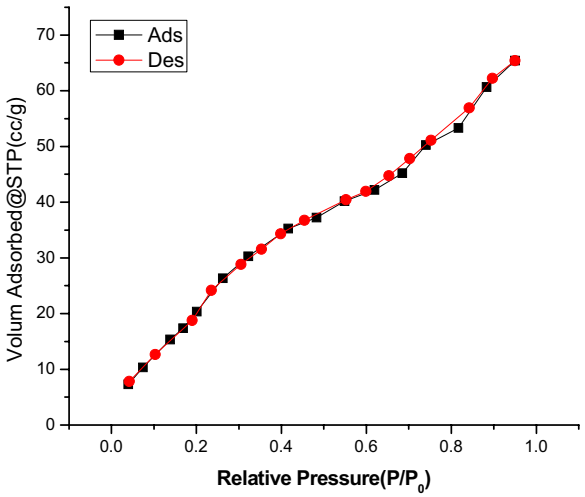

Fig. 3 N_2-adsorption/desorption isotherm of CF-NGs nanograins

2.2.2 Examination of Specimens

After 3, 7, 14, and 28 days, the samples were used for compressive capacity trials using a Ton-industry machine (West Germany) equipped with a 60-ton load cell. Additionally, all of the geopolymeric samples conducted a variety of evaluations of hydration parameters, such as the free portlandite contents (CaO, %), and non-evaporable water content (NW, %). A typical empirical relationship for free portlandite contents (CaO, %) can be expressed as.

$$\text{CaO}, \% = \text{W}(\text{V} \times \text{N} \times 56.08) \times 100,$$

where W = weight of the sample being analyzed (in grams), V = volume of hydrochloric acid (HCl) used in

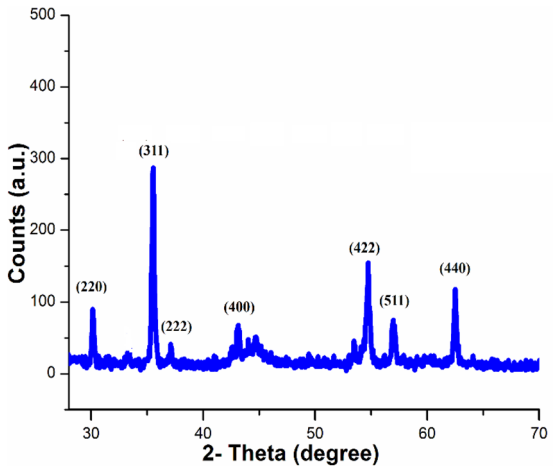

Fig. 4 XRD pattern of CF-NGs nanograins

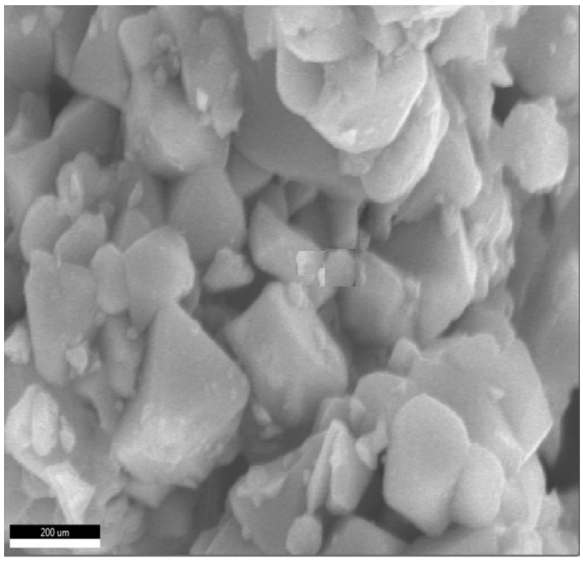

Fig. 5 SEM image of $CuFe_2O_4$ spinel nanograins

Table 2 Contents of the multiple blends and their notations

Mix	Mix proportions, mass%			
	SG	ASA	(CF-NG)	SS/SH
P	100	–	–	1.5
PCF0.5	100	–	0.5	1.5
PCF1	100	–	1.0	1.5
PCF1.5	100	–	1.5	1.5
PS1	95	5	–	1.5
PS1CF0.5	95	5	0.5	1.5
PS1CF1	95	5	1.0	1.5
PS1CF1.5	95	5	1.5	1.5
PS2	90	10	–	1.5
PS2CF0.5	90	10	0.5	1.5
PS2CF1	90	10	1.0	1.5
PS2CF1.5	90	10	1.5	1.5
PS3	80	20	–	1.5
PS3CF0.5	80	20	0.5	1.5
PS3CF1.5	80	20	1.0	1.5
PS3CF1.5	80	20	1.5	1.5

the titration (in milliliters), N = normality of the hydrochloric acid (i.e., its concentration in equivalents per liter), 56.08 = the molecular weight (molar mass) of calcium oxide (CaO) in g/mol. The CaO, %, values were determined by applying the procedures described in the earlier paper (Abo-El-Enein et al., 2018).

Also, a typical empirical relationship for non-evaporable water content (NW, %) can be expressed as :

$$NW.\% = \left[\left(Wi - Wf\right)/Wf\right] \times 100,$$

where *Wi* = mass of dried samples and *Wf* = mass of ignited specimens.

The evaluated specimens are immersed in a strong solution of 5% Na_2SO_4 and 5% $MgCl_2$ for up to 90 days after curing for 7 days under faucet water (as zero time) at 20 °C in order to test their resistance to harsh attack solutions according to ASTM C1012 (Heikal et al., 2020a).

2.2.3 Radiation Measuring Techniques

Gamma attenuation parameter for all OPC-ASA composites were measured experimentally using a collimated beam of ^{137}Cs and ^{60}Co gamma-ray sources. The gamma dose rate was detected by $3' \times 3'$ amplifier NaI (Tl) detector, which was connected to a multi-channel analyzer. Spectra obtained were analyzed using Genie software. The geometrical arrangement of gamma ray's measurement system is constant during all irradiation experiments, as shown in Fig. 6. The spectra were recorded and analyzed by Genie software. For each measurement, to ensure that the statistical error was less than 1%, the detection time was set at 300 s, and background counts were kept at identical durations.

2.2.4 Gamma Attenuation Parameter

The LAC, MAC, HVL, TVL and MFP parameter will be determined for the investigated composites at different energies by the radiation transmission. When a beam of gamma rays with intensity I_0 propagate through a material of thickness x, the intensity will be attenuated according to, (Jia et al., 2016):

$$I(x) = I_0 e^{-\mu x}, \quad (1)$$

where μ is the linear attenuation coefficient (LAC). When gamma attenuation depends on the material density ρ, then it is necessary to determine the total mass attenuation coefficient MAC (μ/ρ) (Bozkurt, 2021) by:

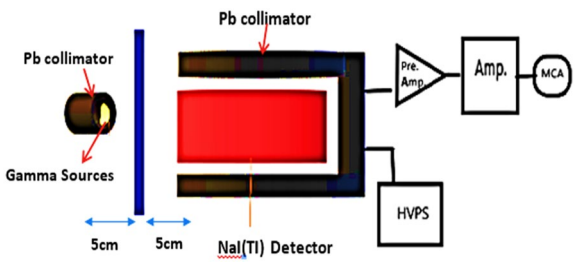

Fig. 6 The gamma-ray measurement system's geometrical configuration

$$\mathrm{MAC} = \frac{\mu}{\rho} = \frac{\ln\left(\frac{I_0}{I}\right)}{\rho x}. \quad (2)$$

The half- and tenth-value layer (HVL, TVL) and the mean free path MFB are determined from:

$$\mathrm{HVT} = \frac{0.693}{\mu} \quad \mathrm{TVL} = \frac{2.303}{\mu} \quad \mathrm{MFP} = \frac{1}{\mu}. \quad (3)$$

For a mixer $\frac{\mu}{\rho} = \sum_i w_i \left(\frac{\mu}{\rho}\right)_i$ (Sallam et al., 2020), where ρi and (μ/ρ)i are the partial density (the density as it appears in the mixture) and the mass attenuation coefficient of the ith constituent, respectively, and w_i is the weight fraction.

For predicting how photons and molecules will interact, the Z_{eff} parameter is crucial. For a variety of energy levels, Zeff's shielding parameters have therefore been computed. The Z_{eff} values for total photon interactions are determined using the formula below: Sallam et al., 2020):

$$Z_{eff} = [\mathrm{MAC} / (\mathrm{NA}\ \Sigma \mathrm{i}\ \mathrm{Wi}\ \mathrm{Ai})]/[\frac{1}{\mathrm{NA}}\ \Sigma\ \mathrm{Fi}\ \mathrm{Ai}\ \mathrm{Zi}(\mathrm{MAC})\mathrm{i}], \quad (4)$$

where N_A is Avogadro s number, A_i and Z_i is the atomic weight and atomic number, respectively, of the elemental composition and f_i is the fractional values of the elements.

The N_{eff} is used to determine the electronic field's effective-density number which it represents the number of electrons per unit mass of the interacting matter and given by:

$$N_{eff} = N_A Z_{eff} / \Sigma_i f_i A_i (\text{electrons / g}). \quad (5)$$

The Phy-X/PSD program is used to investigate the photon attenuation characteristics at photon energies of 0.1–10 MeV. Numerous properties, such as LAC, MAC, HVL, MFP, Z_{eff}, N_{eff} and effective conductivity (C_{eff}), were calculated and compared with the experimental results. This calculation will be useful for comprehending how SG-ASA and the concentration of the replacement affect gamma shielding characteristics.

3 Results and Discussion

3.1 Non-evaporable Water Content (NW, %)

The results for the non-evaporable water content (N_w, %) of hardened geopolymer pastes that were hydrated for up to 28 days are illustrated in Fig. 7A–E. The findings demonstrate that for every analyzed sample, N_w values increased, rising steadily and gradually until the 28-day hydration age. This is because all hardened geopolymer pastes undergo a constant hydration process that releases $Ca(OH)_2$ that creates more hydration yields (Ibrahim et al., 2023b).

ASA up to 20% by mass in mixes PS1, PS2 and PS3, respectively, created a small increase in N_w values in SG-ASA pastes compared to the uncured mix (P) over the entirety curing dates. Because of ASA's high pozzolanic activity, this can be explained (Algamal et al., 2019). At later ages (28 days), the pozzolanic reaction and/or alkaline activation geopolymer binder are triggered by the release of Al^{3+}, Si^{4+}, and Ca^{2+} cations caused by the disintegration of SG when the content of ASA is increased (Heikal et al., 2020a).

Figure 7B–E shows how the inclusion of CF-NGs affected the $N_{W,}$ % values of several reinforced composites over the hydration stages. According to the findings shown in Figure 7B–E, the (N_W) contents showed an increasing trend up to 1.5 mass % CF-NGs. This is because CF-NGs-nanograins are present and act as nucleation nuclei for the hydration process, speeding up the hydration of cement granules (Ibrahim et al., 2023a).

3.2 Gel/Space Ratio (*X*)

As seen in Fig. 8A–E, the (X) ratio grew with hydration times for all series of SG, SG-ASA, and SG-ASA-CF-NGs hardened geopolymer pastes. This results from the buildup of extra C-F-S-Hs, C-S-Hs and C-F-Hs within the pores structure causing a closed matrix system (Heikal et al., 2020b).

Because of the higher pozzolanic power of ASA at later ages, Fig. 8A displays an upward trend with ASA content up to 20%. (Heikal et al., 2020a).

In comparison to the other composite pastes, the (X) values for the various mixtures comprising CF-NGs showed a larger rise. This is explained by the fact that CF-NGs have a larger pozzolanic power, which speeds up the rate of hydration and produces more hydration products (Mohamed et al., 2022a, 2022b). Moreover, higher (X) ratio values were obtained when 1.5 mass% of CF-NGs was added to mix PS3CF1.5 in comparison to the reference sample.

3.3 Compressive Strength

Figure 9A–E displays the compressive strength (Cs) findings for the geopolymer pastes that were cured under various time intervals. As seen in Fig. 9A–E, all specimens exhibited significant enhancement in compressive capacity as the treating period was prolonged. This could be the outcome of a continual advancement in the procedure of hydration over time, leading to the creation of hydration yields among cement particles, filling open pores, and subsequently increasing the gel-to-space ratio, enhancing mechanical features (Ibrahim et al., 2023b). Moreover, the compressive capacity increased with the

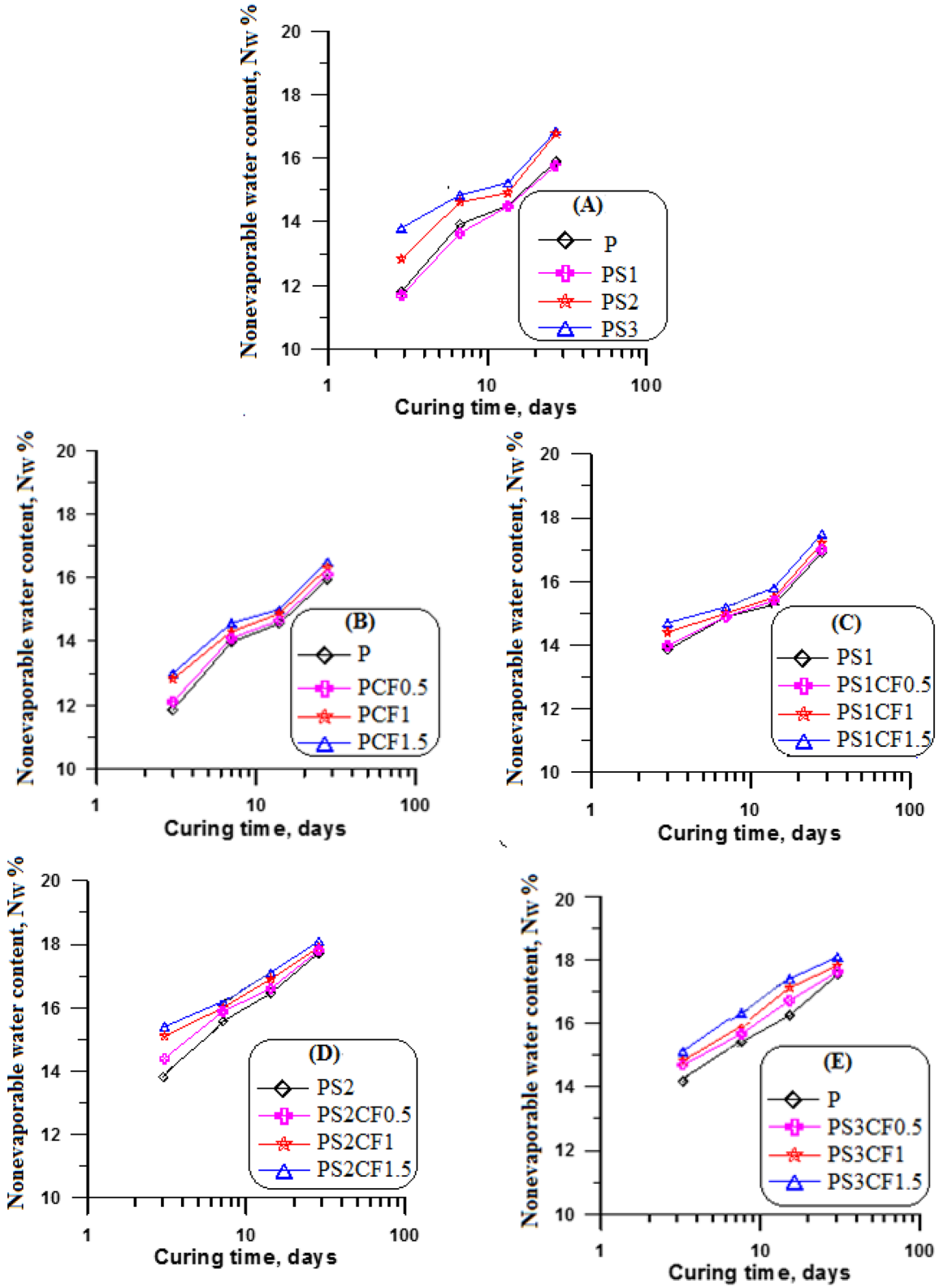

Fig. 7 Non-evaporable water content (NW %) of SG- ASA-CF geopolymer pastes at different curing times

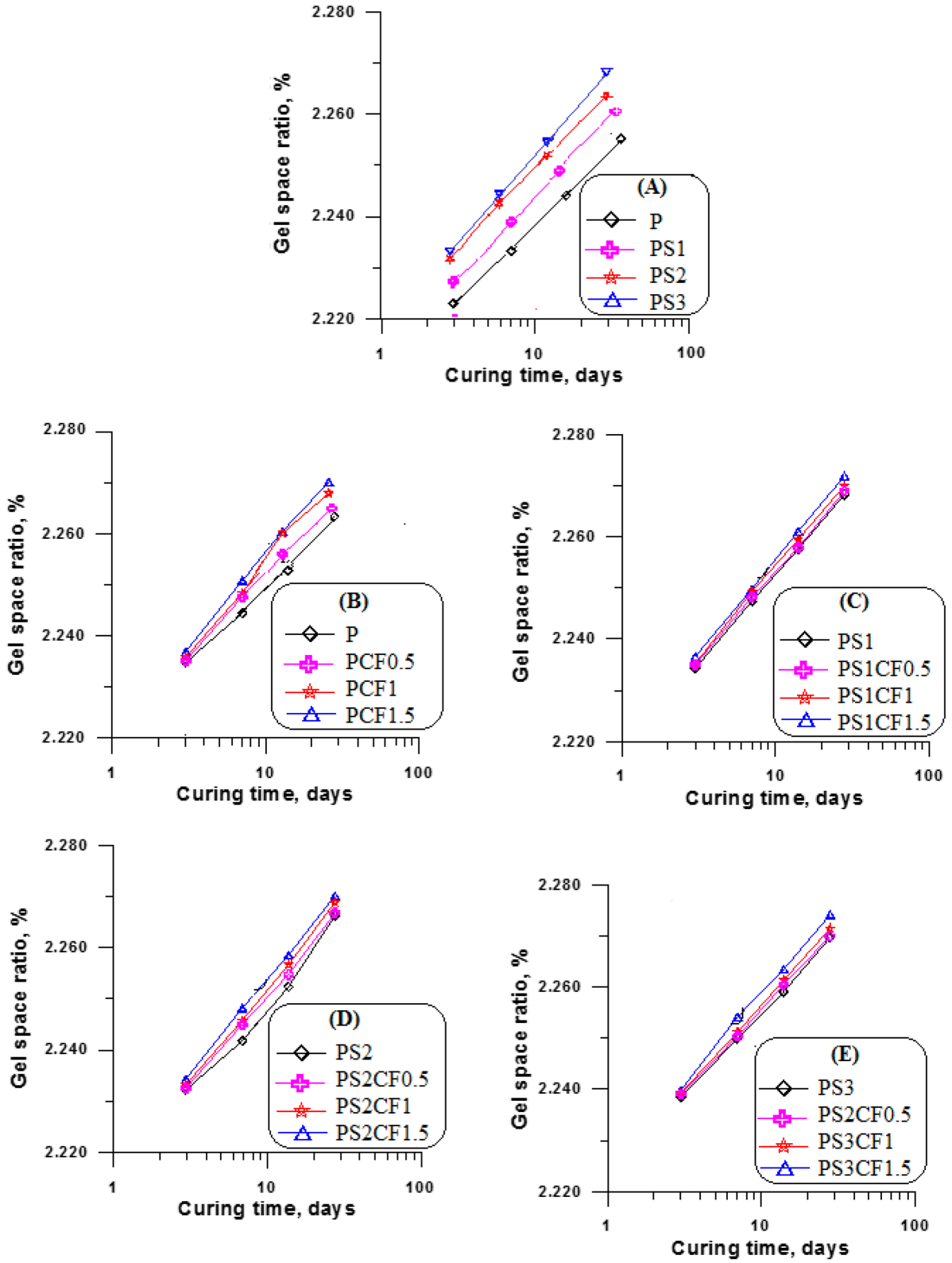

Fig. 8 Gel/space ratio (*X*) for reinforced geopolymer pastes at varying curing times

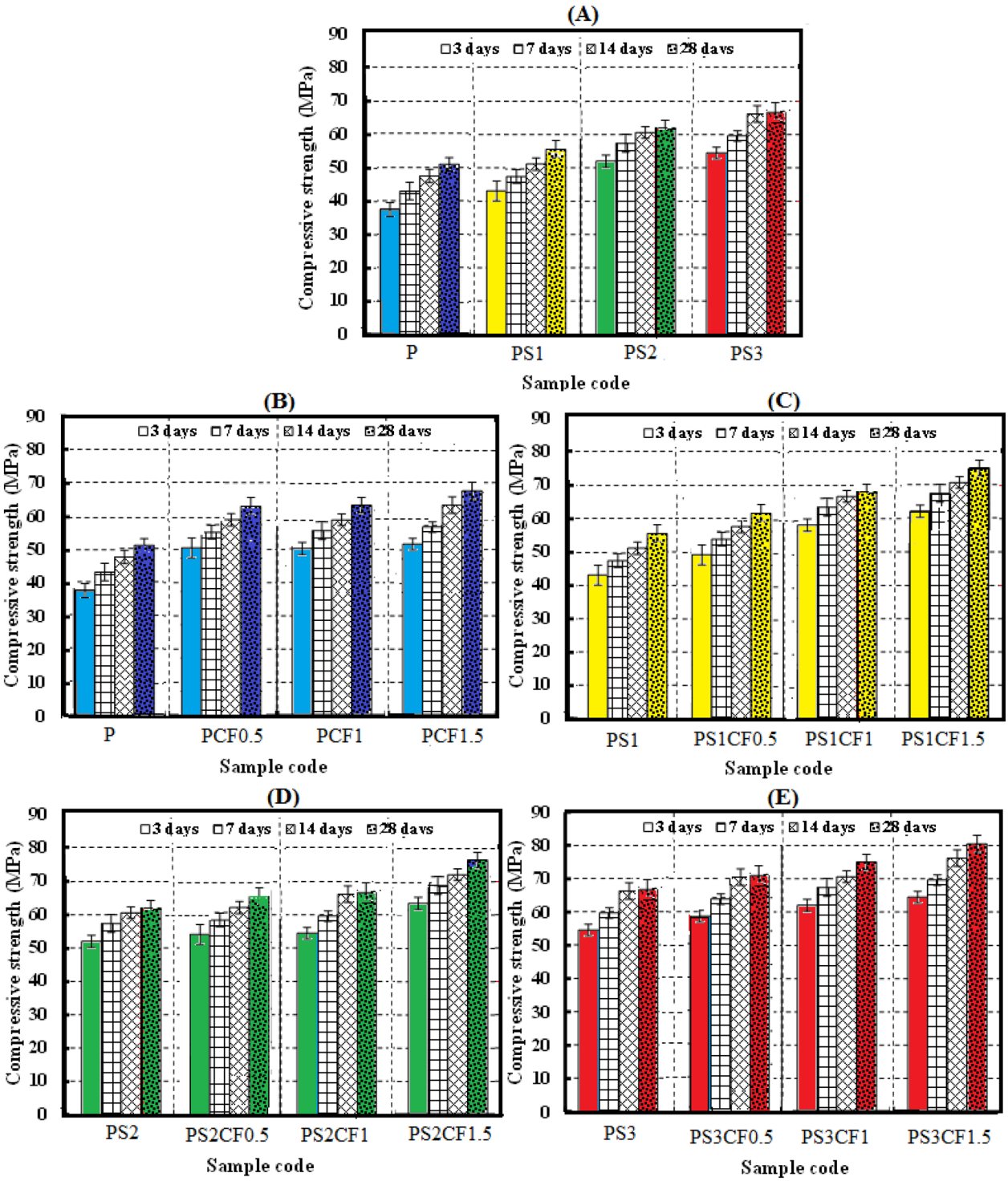

Fig. 9 Compressive strength of hardened SG-ASA-CF geopolymer pastes at different curing times

increase of ASA content up to 20%, which is ascribed to the formation of hydration yields as CASHs, CSHs along with more NASHs gel that could be deposited in the pores of the system owing to the presence of ASA which gave an additional source of aluminosilicate hydrates (Chen et al., 2024; Ferone et al., 2019; Santosa et al., 2019). The optimal replacement ratio of slag-based geopolymer (SG-Geo) by ASA is 20%, as confirmed by the Cs

results; the researcher has already reported this finding (Duan et al., 2022a).

Additionally, in comparison to the uncured sample (mix P), the Cs values were increased for all reinforced composite pastes including 0.5%, 1%, and 1.5% CF-NGs. This is explained by the increased pozzolanic power of CF-NGs, which enhanced the degree of hydration process and generated surplus hydration yields like CAH and CSH in addition to creating novel phases including CFSHs, CuSHs, and CFHs. Additionally, CF-NGs' filling effect in the cement matrix blocks pores among cement grains, increasing the CC magnitudes (Gharieb et al., 2023; Mohamed et al., 2022b).

The outcomes confirmed that the 80% SG–20% ASA–1.5% CF-NGs composite (Mix PS3CF1.5) showed the greatest Cs magnitudes when compared to all other assessed nanocomposites at nearly all trial ages, making it the best option for general building applications.

Consequently, the results of the compressive strength (Cs) and the data gathered through the non-evaporable water contents (N_W, %) are in agreement.

3.3.1 Empirical Modeling of Compressive Strength Development

Empirical equations were established to represent the compressive strength (Cs, MPa) of the geopolymer composites as a function of curing age (*t*, days). Using second-order polynomial regression, the experimental data for various doses of CF-NGs were examined. These models illustrate the temporal progression of compressive strength and emphasize the significance of CF-NGs (Table 3).

These characteristics jointly delineate the progression of compressive strength and provide the quantification of the contribution of CF-NGs to the geopolymer matrix over time.

Table 3 Empirical formulas for compressive strength (Cs) at various CF-NGs contents

Blend designation	Empirical formula ($C_S(t) = a \cdot t^2 + b \cdot t + c$)
P (0% CF-NGs)	$-0.0318 \cdot t^2 + 1.723 \cdot t + 10.598$
PCF0.5 (0.5% CF-NGs)	$-0.0364 \cdot t^2 + 1.983 \cdot t + 10.910$
PCF1 (1% CF-NGs)	$-0.0378 \cdot t^2 + 2.099 \cdot t + 11.780$
PCF1.5 (1.5% CF-NGs)	$-0.0382 \cdot t^2 + 2.196 \cdot t + 13.364$
PS3CF1.5 (20% ASA + 1.5% CF-NGs)	$-0.0428 \cdot t^2 + 2.456 \cdot t + 14.676$

$C_S(t)$ is the compressive strength (MPa) at curing age *t* (days), the constants a, b, and c represent the regression coefficients obtained from curve fitting: a represents the nonlinear (quadratic) rate of strength development. b reflects the linear influence of curing time c is the intercept, which corresponds to the estimated initial strength at $t = 0$

Figure 10 demonstrates the beneficial effect of CF-NGs on the pace of strength growth and validates the regression trends employed in the empirical modeling section. These empirical correlations validate the beneficial effect of CF-NGs on the rate of strength development. The fitted models' parabolic shape confirms the observed experimental behavior and is consistent with hydration kinetics. Additionally, the outcomes support the validity of the modeling approach by being in line with earlier findings in the literature. (Ahmed et al., 2022; Hardjito et al., 2004).

3.4 Phase Identification

3.4.1 XRD Exploration

In Fig. 11, the XRD spectra of the P, PS3, PCF1.5, and PS3CF1.5 blends at 28 days of curing age are displayed. All of the samples showed a board hump particularly at 30°–40° 2θ, which could be related to the amorphous CASHs and NASH gels as documented in the previous investigations (Duan et al., 2022a; El-Sawy et al., 2024), and a tiny small peak associated with Al-tobermorite-gel (C-A-S–H, located at 2 Θ = 28.9∘, PDF# 00–020–0452) was also demonstrated (Mohamed et al., 2023b). For all tested samples, the tiny humps at roughly 29.35° 2θ were

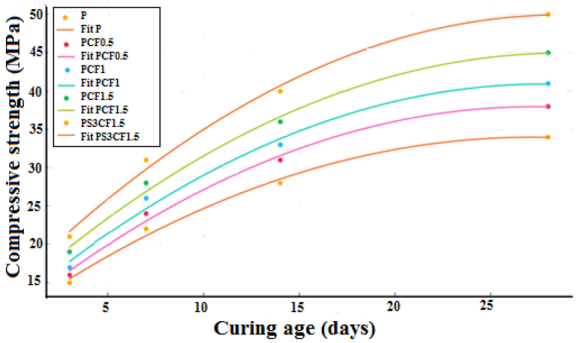

Fig. 10 Experimental compressive strength values and fitted polynomial curves for different CF-NGs contents at various curing ages

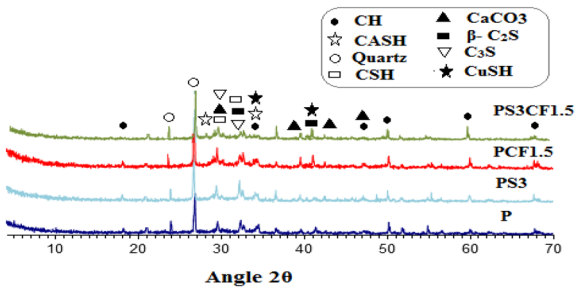

Fig. 11 After 28 days of hydration, the XRD spectrum of the P, PS3, PCF1.5 and PS3CF1.5 blends

attributed to calcium silicate hydrates (CSHs), which could possibly overlap with $CaCO_3$ and C_3S phases. Different diffraction peaks for calcium hydroxide (CH), known as Portlandite, are visible in the XRD patterns of geopolymer pastes (PDF: 00–004-0733). At $2\theta = 18.07°$, 34.06°, 47.13°, and 50.78°, these peaks can be found. For unreacted silicates, specifically C_3S and β-C_2S, specific diffraction peaks can be found at $2\theta = 32.14°$ and 32.47°. The differentiation between C-A-S–H, C-S–H (I), and C-S–H (II) was based on the position and shape of the broad humps and low-intensity reflections observed in the 2θ range of 27°–34°, as referenced in previous studies (Duan et al., 2022a; Mohamed et al., 2022a, 2023b; Rashad et al., 2023). This study follows the criteria described in Taylor (1997); I. G. & Richardson, 2008; Yu et al., 2015; Nonat, 2004), where C-S–H (I) typically shows a broad peak around $2\theta \approx 29°$, while C-S–H (II) exhibits a peak shift toward $2\theta \approx 32°$, indicating a higher degree of structural organization. Additional quantities of CASH, CSH (I), and CSH (II) were formed when 1.5% CF-NGs were added to these composites (Mixes PCF1.5 and PS3CF1.5). Additionally, the dispersion of CF nanograins and their pozzolanic reaction with CH released from polymerization reaction results in the formation of additional phases, specifically CuSH (Mohamed et al., 2022a).

3.4.2 FT-IR Spectroscopy

In Fig. 12, the FT-IR patterns of hydration products of the P, PS3, PCF1.5, and PS3CF1.5 blends at 28 days of curing age are displayed. The stretching and bending vibrations of the O–H groups of H_2O within C-S–H gels are associated with the absorption bands located at 3700—3200 cm^{-1} (Bouchikhi & Y. M-Pajany et al., 2021). Calcite, which may have developed as a result of the pastes' carbonation, is responsible for the band at ~ 1400 cm^{-1}(Burciaga-Díaz et al., 2020). The Si–O stretching vibration of C–S–H Type I—a high-density, well-ordered hydration product is the cause of the band's intensity in the region of 950–1100 cm^{-1} (Abdollahnejad et al., 2019). Additionally, peaks observed at ~ 713 cm^{-1} and ~ 855- 875 cm^{-1} are attributed to Al–O bending modes, suggesting the coexistence of C–A–S–H phases. The intensity of the band at 457–524 cm^{-1} is due to the bending vibrations of O–Si–O and Si–O–Si bonds (Tran et al., 2024). These results demonstrate that the PS3CF1.5 has undergone more complete hydration and developed a more advanced microstructure compared to the P, PS3, and PCF1.5 blends.

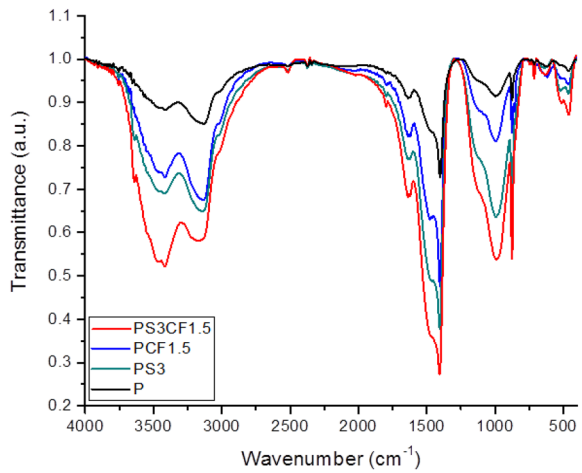

Fig. 12 After 28 days of hydration, the FT-IR patterns of hydration products of the P, PS3, PCF1.5, and PS3CF1.5 blends

3.5 Morphology

Scanning electron microscopy (SEM) was performed to examine the microstructural characteristics of the geopolymer matrix and to evaluate the effects of incorporating alumina sludge ash (ASA) and $CuFe_2O_4$ spinel nanograins (CF-NGs) on morphology, porosity, and densification. In Fig. 13(A–D), SEM images of the tested samples P, PS3, PCF1.5, and PS3CF1.5 at 28 days of curing age showed that the main hydration products were CASHs and CSHs. As demonstrated in Fig. 13(A), the control geopolymer matrix (P) exhibited a heterogeneous microstructure with visible micro-cracks and a relatively porous matrix. In comparison to the control sample (P), the SEM pictures of PCF1.5 nanocomposites in Fig. 13B showed promoted homogeneity and an improved compact microstructure with significantly fewer pores and unreacted particles, as a result of the CF-NGs acting as binder, fillers, and nucleation sites for the resulting yields, enhancing the compressive capacity (Gharieb et al., 2023). Figure 13C reveals the formation of a dense microstructure, which improved the microstructural compactness owing to the pozzolanic action of ASA (Mohamed et al., 2022b). Among all the blends, the generation of extra hydration yields and/or the formation of new products like CuSH is the key factor for the dense structure and hard matrix of PS3CF1.5 nanocomposites as shown in Fig. 13D. Moreover, the enhanced interfacial bonding and packing between the nanograins and the geopolymer gel led to microstructural densification, which is consistent with the noted improvements in gamma radiation shielding and mechanical strength. These results offer compelling microstructural evidence in favor of the suggested processes and the macro-scale performance gains. Thus, the complementary evidence from XRD and SEM, collectively confirms that the incorporation of CF-NGs and ASA not only improves the structural integrity of the geopolymer matrix, but also promotes the formation of

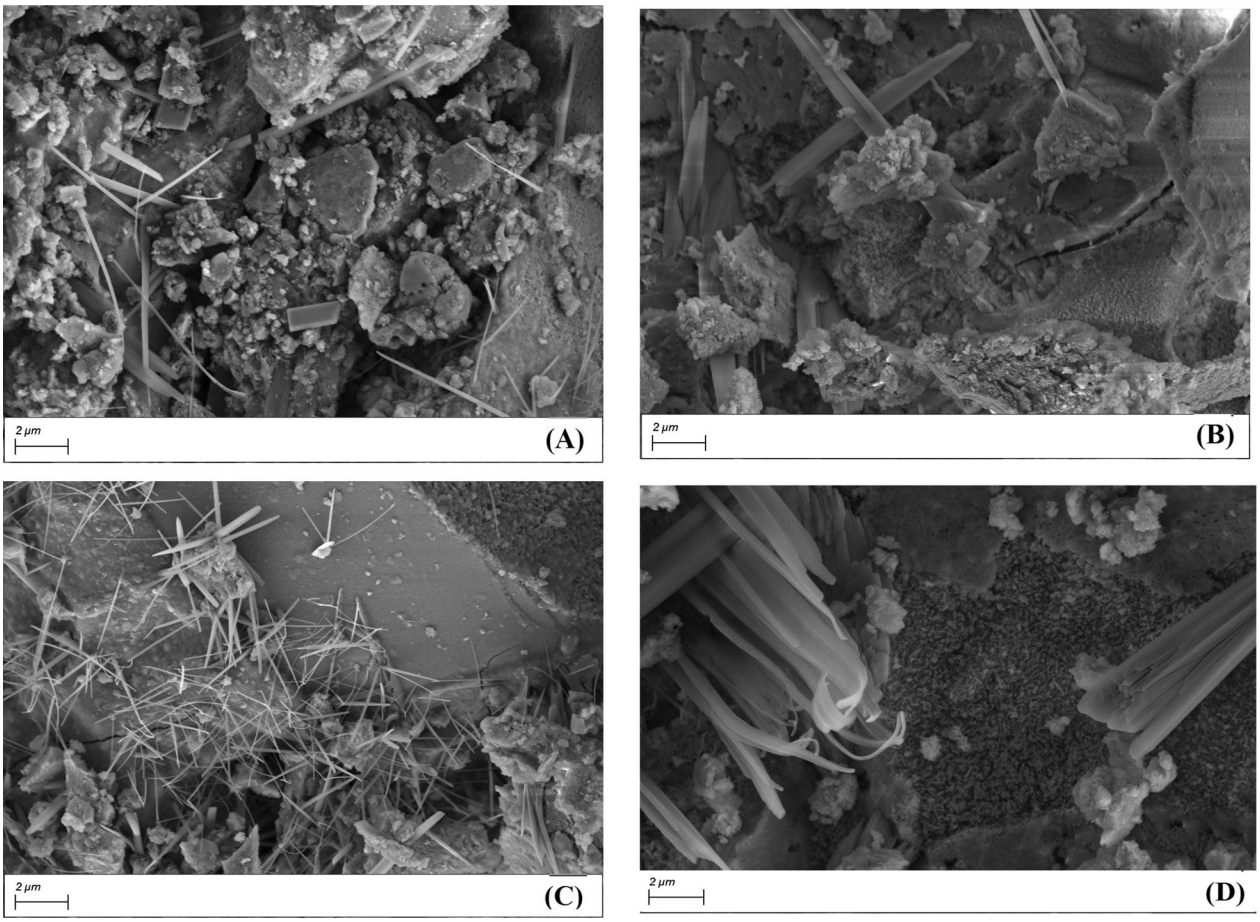

Fig. 13 After 28 days of hydration, the SEM images of the P, PS3, PCF1.5 and PS3CF1.5 blends

stable and compact gel phases, which enhance both durability and radiation shielding effectiveness.

3.6 Assessments of Durability Against Aggressive Environments

3.6.1 Aggressive Sulfate and Chloride Attack

4 Compressive Strength (Cs)

The compressive strengths of test specimens submerged in 5% Na_2SO_4 solution or 5% NaCl solution for up to 90 days are displayed in Figs. 14, 15(A–E). The results reported that the compressive strength of all tested specimens developed with the progress of soaking time up to 90 days as the result of the growth of hydration yields with increasing curing time (Mohamed et al., 2023a). The results in Figs. 14, 15(A–E) reveal that plain (mix P) compressive strength decreased in comparison to mixes PS1, PS2, and PS3 up to 90 days of soaking in a 5% Na_2SO_4 solution. Although the strength loss was less than that caused by sulfate, similar outcomes were seen for geopolymer pastes soaked in 5% NaCl solution (Fig. 14); this may be attributed to the entry of SO_4^{-2} ions into the matrix system, which leads to the creation of ettringite (Aft) and gypsum ($CaSO_4$), which is typically the cause of the specimens' decreased strength depending on the amount of tricalcium aluminate and CH in the structure, while the enhancing in the strength of the specimens soaked in chloride solution was as a result of the acceleration of the early hydration process occurring in chloride solution (He et al., 2024). This performance is directly related to the pore features due to the presence of up to 20% ASA replacement ratio, which results in the creation of more C-S-H hydrates that are deposited in the accessible pores and reduces porosity, increasing compactness and effectively prevents the penetration of salt solutions into the matrix system (Owaid et al., 2019). Moreover, adding adequate amounts of ASA can reduce ASR gel content owing to the reality that ASA consumes the Portlandite developed upon hydration, diminishing the potential of creating ASR gels. Thus, with the ASA content increased by up to 20% of substitution, the Cs

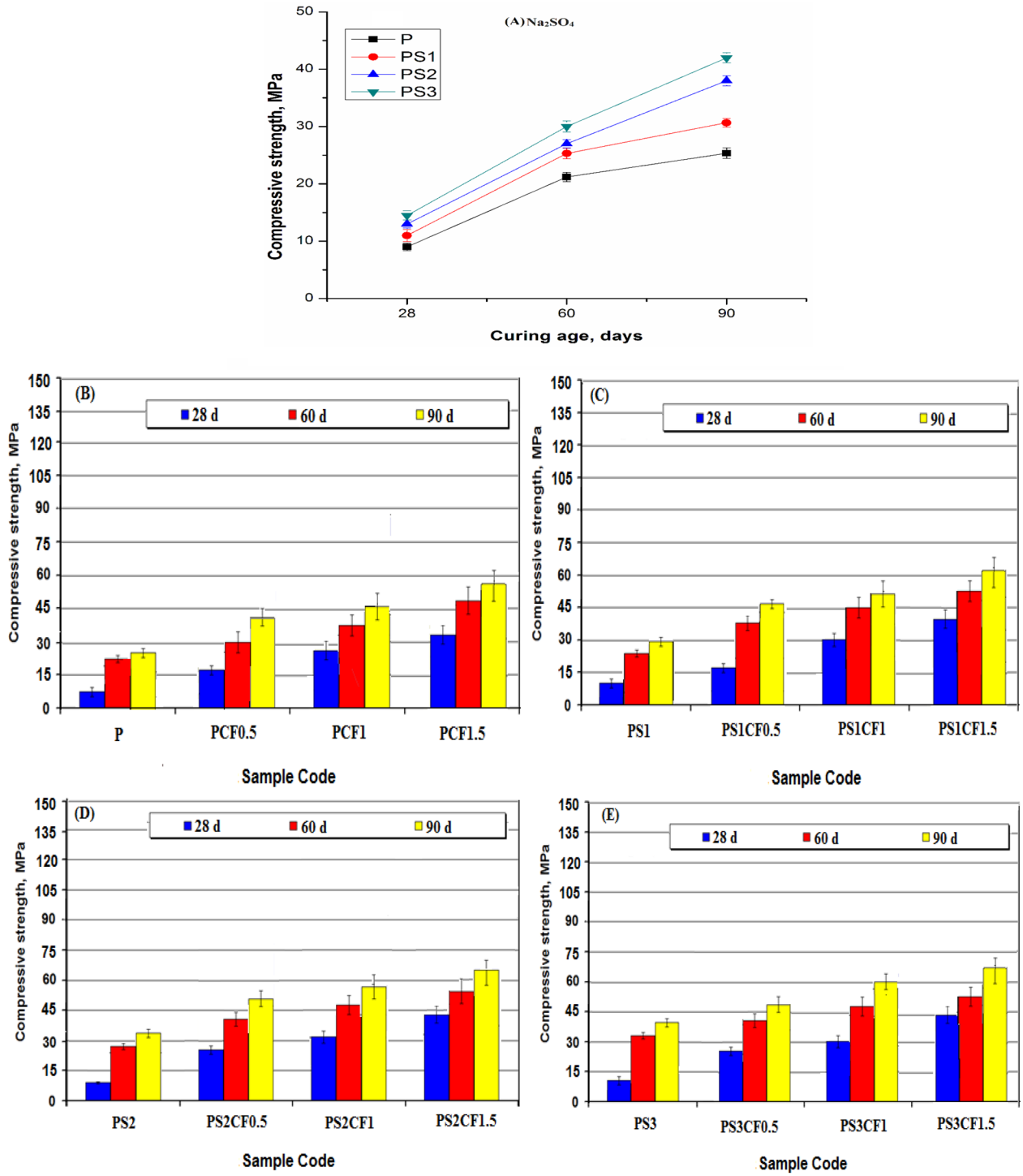

Fig. 14 Cs of activated SG-ASA-CF binders and a reference specimen immersed in 5% Na_2SO_4 solution up to 90 days

magnitudes of SG-ASA hardened geopolymer composites are enhanced (Duan et al., 2022c).

By adding $CuFe_2O_4$ spinel nanograins (CF-NGs) at varying weight percentages (0.5%, 1%, and 1.5% by weight), the reaction of ASA with portlandite is promoted to create massive yields of CSHs and N(C)ASHs geopolymeric gel in the matrixes, which accumulate in the larger pore-spaces, reducing porosity and thus hindering the

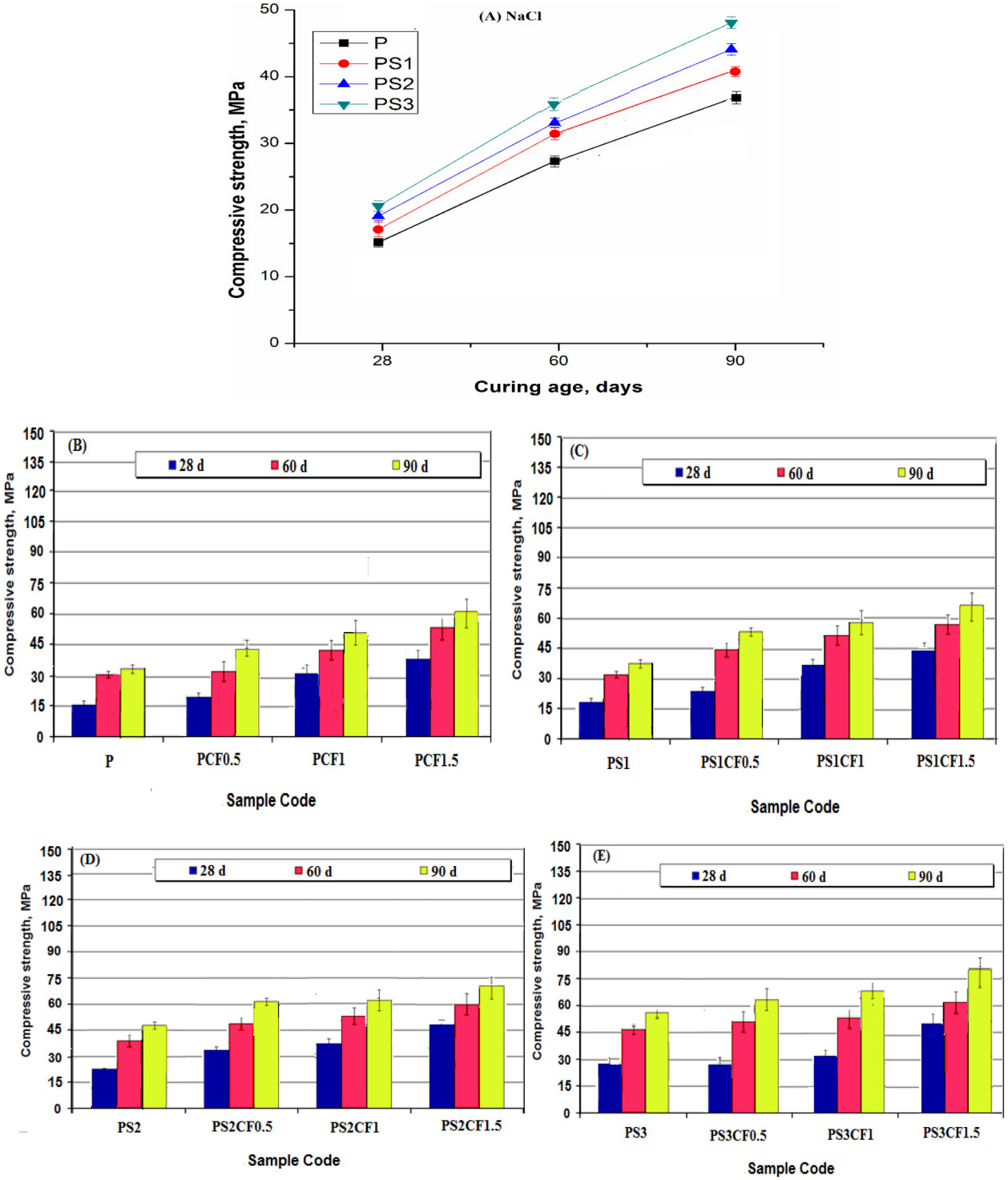

Fig. 15 Cs of activated SG-ASA-CF binders and a reference sample immersed in 5% NaCl solution up to 90 days

attendance of Cl^{-1} and/ or SO_4^{-2} ions in the available open pores, thus reducing the decay action of the structure matrix and enhancing the CS (He et al., 2024; Heikal et al., 2020a). While the magnitudes of Cs of PS1, PS2, and PS3 mixes are increased, respectively, in the same order in the presence of CF nanograins in the matrices, as shown in Figs. 14 and 15A, Mix P exhibited lower

rates of Cs than other mixes at all ages submerged in 5% Na_2SO_4 solution or even 5% NaCl solution.

It is generally observed that for all investigated mixes, the enforcement effect of CFs-NGs rises with increasing addition doses (from 0.5 to 1.5%), as seen by an increase in the Cs magnitudes. This improvement is credited to the CFs NPs' filling action, which encouraged the geopolymer matrix's porosity to decrease and impede the presence of Cl^{-1} and/ or SO_4^{-2} ions in the available open pores, hence lessening the geopolymer matrix's deterioration influence (Mohamed et al., 2022b). As clarified in Figs. 14 and 15(B–E), (Mix PS3CF1.5) exhibited the greatest Cs values when compared to all other tested nanocomposites under the same curing circumstances, making it the best option for durability against aggressive environments used for building applications.

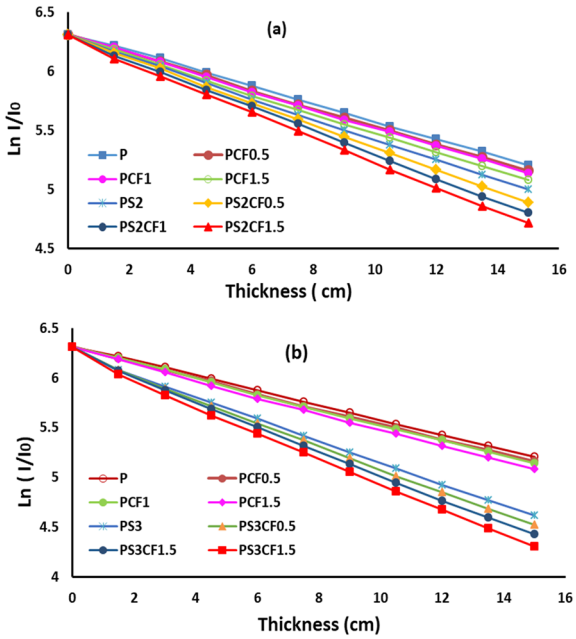

Fig. 16 The variation of gamma linear attenuation as a function of the thickness for different concentration of composites (SG-ASA-CF NGs). **a** At ASA replacement ratio of 10%. **b** At ASA replacement ratio of 20%

4.1 Radiation Shielding Performance

Figure 16(a, b) describes the attenuation efficiency for ^{137}Cs and ^{60}Co gamma radiation detection, respectively, for the 12 SG-ASA composites with different concentration of additives as given in Table (2). In these figures, every point of data reflects the mean of seven different measurements. The variations in the recorded gamma doses are the primary cause of the about 5% measurement uncertainty. The attenuation data demonstrate that as composite thickness increases, the gamma-ray equivalent dose decreases exponentially. For each composite type, the LAC for gamma rays was determined experimentally from the attenuation curves in Fig. 16(a, b) and presented in Tables 4 and 5, using Eq. (1). The concentration of ASA was found to have an impact on the attenuation of gamma rays, particularly for PS3CF1.5 with 1.5% of CF-NG. This composite's relatively thin thickness was needed to attenuate gamma rays more than other composites showed.

As illustrated in Fig. 17, the LAC values of the samples were derived from experimental measurements at

Table 4 Mass attenuation coefficient (MAC) for the 12 SG-ASA composites that determined experimentally and compared with Phy-X program results

Sample	Mass attenuation coefficient, cm 2/g					
	Experimental			Theoretical		
	0.662 MeV	1.17 MeV	1.33 MeV	0.662 MeV	1.17 MeV	1.33 MeV
P	0.07709	0.05867	0.05498	0.07713	0.05912	0.0556
PCF0.5	0.07712	0.05869	0.05497	0.07714	0.05915	0.05562
PCF1	0.07716	0.05872	0.05496	0.07718	0.05918	0.05565
PCF1.5	0.07718	0.05874	0.05494	0.07720	0.0593	0.05567
PS2	0.07724	0.05876	0.05497	0.07725	0.05934	0.05569
PS2CF0.5	0.07728	0.05878	0.05495	0.07729	0.05937	0.05571
PS2CF1	0.07730	0.05882	0.05494	0.07733	0.05939	0.05572
PS2CF1.5	0.07732	0.05886	0.05493	0.07737	0.05942	0.05575
PS3	0.07738	0.05889	0.05495	0.07742	0.05947	0.05579
PS3CF0.5	0.07745	0.05892	0.05494	0.07746	0.05949	0.05583
PS3CF1.5	0.07750	0.05895	0.05493	0.07753	0.05953	0.05586
PS3CF1.5	0.07753	0.05898	0.05491	0.07758	0.05958	0.05588

Table 5 The values of HVL, TVL and MFP for the 12 SG-ASA composites at different energies

Composite	0.662 MeV			1.17 MeV			1.33 MeV		
	HVL	TVL	MFP	HVL	TVL	MFP	HVL	TVL	MFP
P	3.877	12.879	5.593	5.0754	16.860	7.3225	5.373	17.849	7.752
PCF0.5	3.854	12.804	5.560	5.0484	16.770	7.283	5.344	17.755	7.711
PCF1	3.817	12.676	5.505	5.0232	16.687	7.247	5.326	17.690	7.683
PCF1.5	3.777	12.547	5.449	5.003	16.620	7.218	5.297	17.596	7.642
PS2	3.677	12.215	5.304	4.812	15.982	6.941	5.212	17.315	7.519
PS2CF0.5	3.636	12.078	5.245	4.781	15.881	6.897	5.145	17.093	7.423
PS2CF1	3.611	11.995	5.209	4.745	15.762	6.846	5.079	16.875	7.329
PS2CF1.5	3.578	11.886	5.162	4.661	15.479	6.722	5.003	16.618	7.217
PS3	3.543	11.770	5.112	4.6154	15.332	6.659	4.969	16.509	7.170
PS3CF0.5	3.468	11.519	5.003	4.567	15.175	6.590	4.874	16.194	7.033
PS3CF1.5	3.382	11.235	4.879	4.444	14.766	6.413	4.756	15.800	6.862
PS3CF1.5	3.337	11.087	4.815	4.361	14.587	6.335	4.690	15.582	6.767

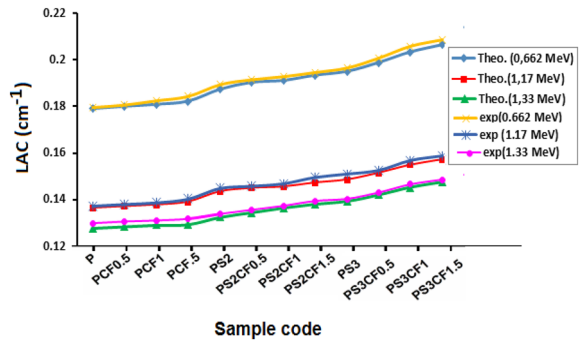

Fig. 17 The linear attenuation coefficients LAC generated from experimental results, and Phy-X/PDS calculations at different energies

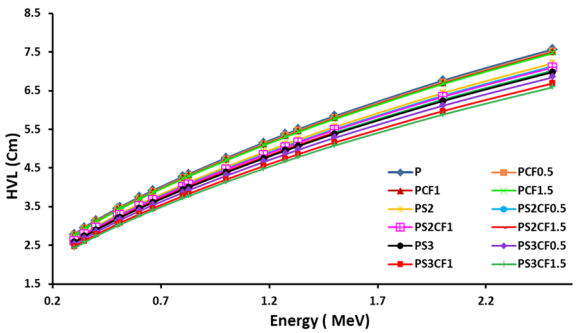

Fig. 18 The halve value layer HVL of the studied composites by Phy-X/PDS at different photon energies

energies of 0.662 MeV, 1.17 MeV, and 1.33 MeV as well as from the Phy-X/PSD software program. As can be seen from Fig. 17, the LAC of the samples is dependent on both the incident gamma ray energy and the ASA concentration as well as depend on sample density as shown in Table (2). The experimental and theoretical values of LAC are closed together and it shows a good degree of consistency, as shown in Fig. 17, with variations ranging from 0 to 8%.

Tables 4 and 5 provide a comparative analysis of some of important shielding properties, such as MAC, HVL, TVL, and MFP, for the SG-ASA samples under examination and represented in Fig. 18, 19.

Figure 19(a, b) illustrates the MAC values at energy range 0.05–2 MeV that were calculated by the Phy-X/PSD software program. Among the examined SG-ASA composites, PS3CF1.5 composite with 1.5% of CF-NG has the highest MAC value of 0.07758 cm^2/ g at 0.05 MeV but, When the energy levels rise, the MAC value decreases to 0.05588 cm^2/g, this can be clarified by the three types of gamma interactions with matter: Compton effect, pair production, and photoelectric effect according to the energy loss or scatters of the incident photon. All SG-ASA composites exhibit photoelectric absorption at around 100 keV as the main effect; MAC looks fairly high and decreases beyond this energy.

Overall, the simulated gamma mass attenuation coefficient values for the SG-ASA composite shields at the selected energies agreed well with the theoretical results that Phy-X software produced. When ASA concentration rises in low energies as opposed to higher energies, it has been observed that the reported mass attenuation coefficient rises as well. This is also caused by the comparatively high density of PS3CF1.5 composite.

The variance in effective atomic numbers (Z_{eff}) and effective electron density (N_{eff}) for the 12 SG-ASA composites under study at various energies is shown in Figs. 20 and 21, and the variation of effective conductivity (C_{eff}) is shown in Fig. 22. The pattern in Figs. 20 and

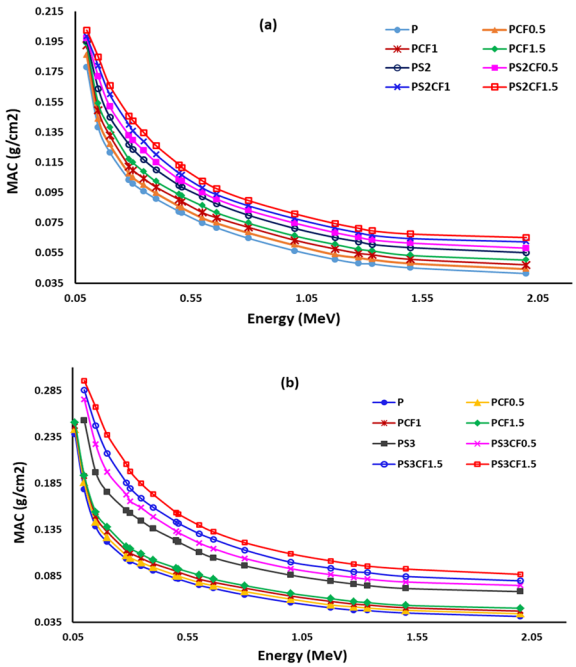

Fig. 19 **a**, **b** Mass attenuation coefficient (MAC) for composites at different energies

21 is similar, showing that as energy increases, both Z_{eff} and N_{eff} drop. In this area, the apparent drop is caused by an increase in the number of excited electrons more photons being ejected as the energy rises. Then, because of the Compton scattering, they stay relatively constant in the medium-energy zone before slightly increasing in the area of high-energy because of the pair creation. Effective conductivity (C_{eff}) is closely related to N_{eff} since it is primarily determined by the quantity of photon energy that collide with electrons and transform them into free electrons. At the same energy range, C_{eff} behaves in the same way as N_{eff} and Z_{eff}, as illustrated in Fig. 23. As given in Fig. 23, N_{eff} and C_{eff} have a direct correlation. Therefore, the composite of SG-ASA that contains 20% (ASA and 1.5% $CuFe_2O_4$ spinel nanograins (CF-NGs) has the highest Z_{eff}, N_{eff}, and C_{eff}, according to the most recent data.

The mean free path (MFP) of the examined SG-ASA mixture at the 0.04–15 MeV photon energy range is shown in Fig. 24. It is clear that the MFP values are directly proportional to photon energies. The reason for this upward trend is that the high-energy radiation can readily pass through the incident material. Photoelectric effects are less dominant than Compton interactions at higher energy. The Compton interactions only occur between incident photons and the outermost electrons of the SG-ASA atoms, and they are barely influenced by energy (E) and atomic numbers because photon attenuation decreases as a result of this alteration. According to the findings in Table 5 and Fig. 24, PS3CF1.5 has the lowest MFP across all energies.

5 Conclusion

The viability of green geopolymer designed using various ASA/SG ratios was examined to assess the mechanical performance, gamma radiation shielding, and durability characteristics against aggressive environments.

This study demonstrates the good shielding behavior and good agreement of the examined SG-ASA composites in detecting the effective electron density (Neff),

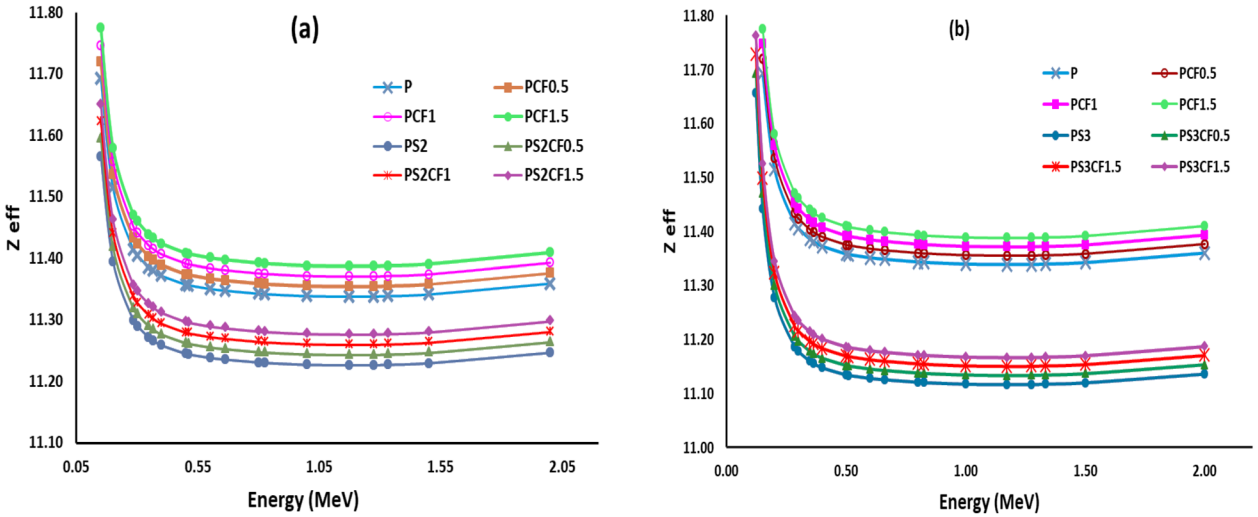

Fig. 20 **a** The variation of effective atomic number Z_{eff} with gamma energies for composites with 0% ASA and composites with replacement 10% ASA. **b** The variation of effective atomic number Z_{eff} with gamma energies for composites with 0% ASA and composites with replacement 20% ASA

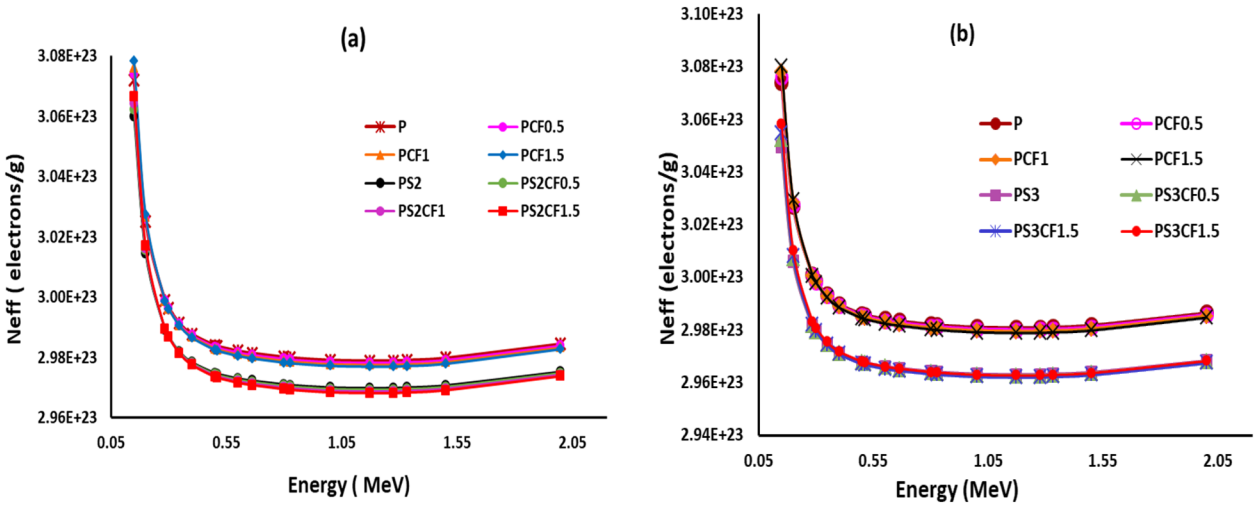

Fig. 21 **a** The effective electrons density N_{eff} as a function with gamma energies for SG-ASA composites with (0% and 10% replacement of sludge). B: The effective electrons density N_{eff} as a function with gamma energies for SG-ASA composites with (0% and 20% replacement of sludge)

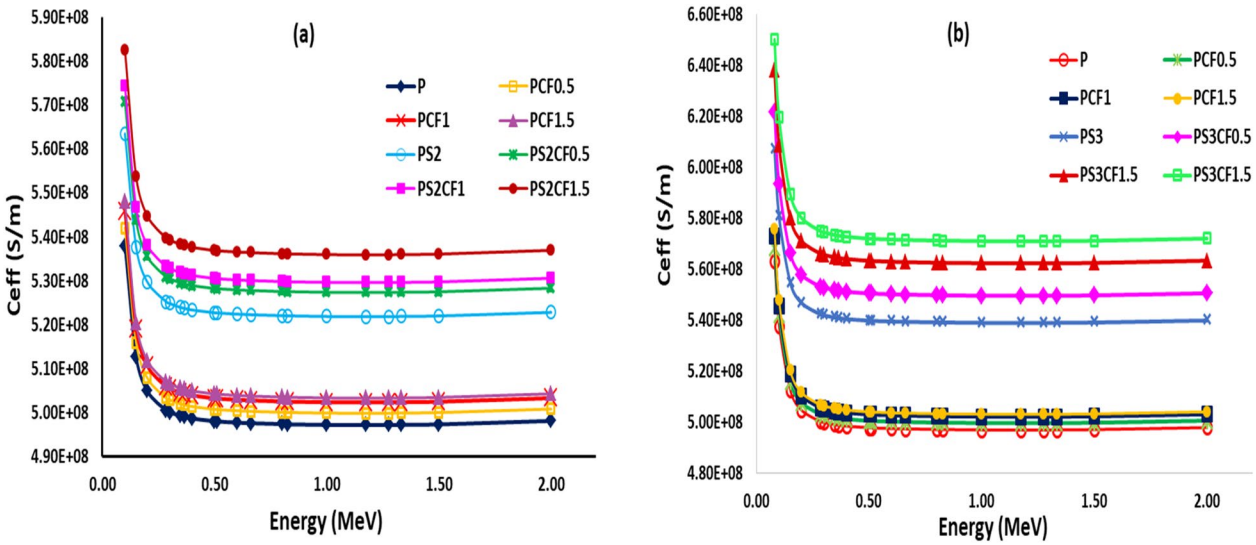

Fig. 22 **a** The variation of effective conductivity C_{eff} with different gamma energy for base composites (0% ASA) compared with composite relapsed 10% ASA. **b** The variation of effective conductivity Ceff with different gamma energy for base composites (0% ASA) compared with composite relapsed 20% ASA

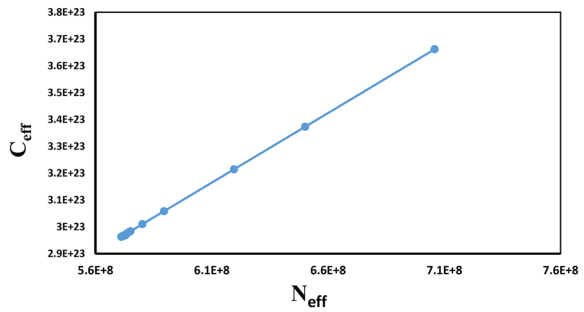

Fig. 23 Effective conductivity (Ceff) and effective electron density (Neff) in relation to PS3CF1.5 composite

effective conductivity (Ceff), HVL, the effective atomic number (Zeff), mass attenuation coefficient (MAC), LAC, TVL, and MFP. Therefore, the studied composites are useful in a variety of shielding applications, especially in radiation facilities, and have good shielding qualities.

Based on the findings, the following inference may be developed:

1. Incorporating thermally treated alumina sludge ash (ASA) as a partial replacement for slag-based geo-polymer at levels of up to 20% (by mass), Mix PS3,

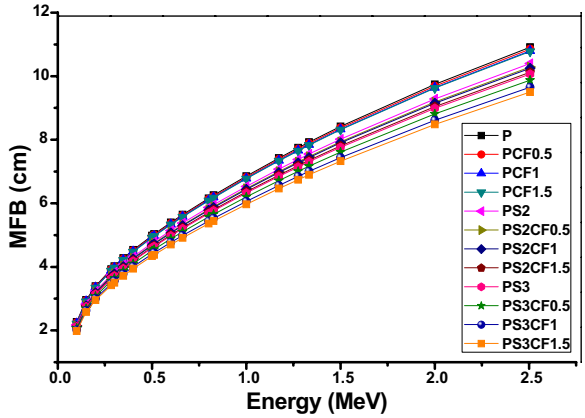

Fig. 24 The variation of mean free path (MFP) at different photon energy for all composites

resulted in an upward trend in the N_W contents and gel/space ratio (X) compared to the uncured Mix (P) over all processing ages.

2. The compressive strength magnitudes were boosted for each of the reinforced composite pastes featuring 0.5%, 1% and 1.5% CF-NGs compared to the uncured specimen (mix P); this related to the occurrence of hydration yields as CASHs, CSHs along with more NASHs gel that could be deposited in the pores of the system
3. The inclusion of 1.5% CF-NGs resulted in an upward trend in the compressive capacity magnitudes compared to their standards (mixes P-PS3) due to the good dispersion caused by CF-NGs spinel nanograins.
4. The incorporation of CF-NGs altered the capacity to resist sulfate aggressive environment. By preventing diffusion via the open holes and lowering the achievable SO_4^{2-}, the geopolymer gel precipitation in the matrix lessened degradation.
5. Comparing cases exposed to Cl^-solutions to those exposed to SO_4^{2-}solutions, the former displayed greater compressive strength values.
6. The shielding efficiency of diverse SG-ASA composites was examined both experimentally and theoretically using the Phy-X/PSD software and Genie software program, which showed a good agreement and good shielding behavior of the studied SG-ASA composites particularly for the mix of (PS3CF1.5) with 1.5% of CF-NG, indicating its superior ability for radiation shielding.

Acknowledgements
The authors are grateful to acknowledge all who have been instrumental in the creation of this review article.

Author contributions
Ola A. Mohamed: conceptualization, writing—original draft preparation, software, data curation, visualization, investigation, software, validation, writing—review and editing. Ahmed Hassan: conceptualization, writing—original draft preparation, investigation, writing—reviewing and editing, data curation, visualization. Nesreen R. Abdelwahab: conceptualization, writing—original draft preparation, software, data curation, visualization, validation, investigation, writing—reviewing and editing. Each author has participated sufficiently in the work to take public responsibility for appropriate portions of the content. All authors read and approved the final manuscript.

Funding
Open access funding provided by The Science, Technology & Innovation Funding Authority (STDF) in cooperation with The Egyptian Knowledge Bank (EKB). This research received no external funding.

Data availability
Some or all data, models, or code that support the findings of this study are available from the corresponding author upon reasonable request.

Declarations

Competing interests
The authors declare that they have no known competing financial interests or personal relationships that could have appeared to influence the work reported in this paper.

Received: 13 March 2025 Accepted: 19 July 2025
Published online: 22 September 2025

References

Abd El-Gawad, W. M., Mossalam, E. A., & Selim, M. M. (2023). Facile preparation of anticorrosive and decorative multifunctional coatings via the inclusion of pearlescent oxide-covered mica pigments. *Journal of Coatings Technology and Research, 20*, 603–622. https://doi.org/10.1007/s11998-022-00693-z

Abd Elwahab, N. R., Helal, N., Mohamed, T., Shahin, F., & Ali, F. M. (2019). New shielding composite paste for mixed fields of fast neutrons and gamma rays. *Materials Chemistry and Physics, 233*, 249–253. https://doi.org/10.1016/j.matchemphys.2019.05.059

Abdollahnejad, Z., Dalvand, A., Mastali, M., Luukkonen, T., & Illikainen, M. (2019). Effects of waste ground glass and lime on the crystallinity and strength of geopolymers. *Magazine of Concrete Research, 71*(23), 1218–1231. https://doi.org/10.1680/jmacr.18.00300

Abo-El-Enein, S. A., El-Gamal, S. M. A., Aiad, I. A., Azab, M. M., & Mohamed, O. A. (2018). Early hydration characteristics of oil well cement pastes admixed with newly prepared organic admixture. *HBRC Journal, 14*(2), 207–214. https://doi.org/10.1016/j.hbrcj.2016.09.001

Ahmed, H. U., Mohammed, A. A., & Mohammed, A. S. (2022). Soft computing models to predict the compressive strength of GGBS/FA-geopolymer concrete. *PLoS ONE, 17*(5), Article e0265846. https://doi.org/10.1371/journal.pone.0265846

Algamal, Y., Khalil, N. M., & Mohammed, M. M. (2019). Statistical design of Portland cement modified with water treatment plant sludge. *IJEAT*. https://doi.org/10.35940/ijeat.F8275.109119

Al-Sughayer, R., Alkhateb, H., Yasarer, H., Najjar, Y., & Al-Ostaz, A. (2024). Evaluation and prediction of slag-based geopolymer's compressive strength using design of experiment (DOE) approach and artificial neural network (ANN) algorithms. *Construction and Building Materials, 440*, Article 137322. https://doi.org/10.1016/j.conbuildmat.2024.137322

Bouchikhi, A., M-Pajany, Y., Maherzi, W., A-Mercier, C., El-Moueden, H., Benzerzour, M., Peys, A., & Abriak, N.-E. (2021). Use of residual waste glass in an alkali-activated binder – Structural characterization, environmental leaching behavior and comparison of reactivity. *Journal of Building Engineering*. https://doi.org/10.1016/j.jobe.2020.101903

Bozkurt, A., & Sengul, A. (2021). Monte Carlo approach for calculation of mass energy absorption coefficients of some amino acids. *Nuclear Engineering and Technology, 53*(9), 3044–3050. https://doi.org/10.1016/j.net.2021.04.004

Burciaga-Díaz, O., Durón-Sifuentes, M., Díaz-Guillén, J. A., & Escalante-García, J. I. (2020). Effect of waste glass incorporation on the properties of geopolymers formulated with low purity metakaolin. *Cement and Concrete Composites, 107*, Article 103492. https://doi.org/10.1016/j.cemconcomp.2019.103492

Chatveera, B., Hengterm, P., Makul, N., & Sua-iam, G. (2024). Enhancing the mechanical and thermal properties of geopolymers prepared by refractory brick dust: An investigation into optimal mix ratios and curing conditions. *Journal of Building Engineering, 94*, Article 110059. https://doi.org/10.1016/j.jobe.2024.110059

Chen, S., Duan, P., Zhao, M., Shi, H., & Bie, Y. (2024). Solidification mechanism and strength characteristics of alkali-activated tannery sludge-slag geopolymer. *Buildings, 14*(4), 1060. https://doi.org/10.3390/buildings14041060

Chinnappa Reddy, B., Vidya, Y. S., Manjunatha, H. C., Sridhar, K. N., Mahaboob Pasha, U., Seenappa, L., Sadashivamurthy, B., Dhananjaya, N., Sankarshan, B. M., Krishnaveni, S., Sathish, K. V., & Damodara Gupta, P. S. (2022). Synthesis and characterization of Barium ferrite nano-particles for X-ray/gamma radiation shielding and display applications. *Progress in Nuclear Energy, 147*, Article 104187. https://doi.org/10.1016/j.pnucene.2022.104187

Duan, S., Guo, H., Sun, H., Zhou, X., Lu, G., Guo, Y., & Ma, Z. (2024). Effect of synthesis conditions on mechanical properties and microstructure of coal gasification slag-based geopolymer. *Construction and Building Materials, 443*, Article 137736. https://doi.org/10.1016/j.conbuildmat.2024.137736

Duan, W., Zhuge, Y., Chow, C. W. K., Keegan, A., Liu, Y., & Siddique, R. (2022a). Mechanical performance and phase analysis of an eco-friendly alkali-activated binder made with sludge waste and blast-furnace slag. *Journal of Cleaner Production, 374*, Article 134024. https://doi.org/10.1016/j.jclepro.2022.134024

Duan, W., Zhuge, Y., Pham, P. N., Liu, Y., & Kitipornchai, S. (2022b). A ternary blended binder incorporating alum sludge to efficiently resist alkali-silica reaction of recycled glass aggregates. *Journal of Cleaner Production, 349*, Article 131415. https://doi.org/10.1016/j.jclepro.2022.131415

Duan, W., Zhuge, Y., Pham, P. N., Liu, Y., & Kitipornchai, S. (2022c). A ternary blended binder incorporating alum sludge to efficiently resist alkali-silica reaction of recycled glass aggregates. *Journal of Cleaner Production*. https://doi.org/10.1016/j.jclepro.2022.131415

El-Sawy, A. A., Heikal, M., Ibrahim, S. M., & Mohamed, O. A. (2024). Experimental and theoretical study on the physico-mechanical characteristics and radiation shielding capability of hardened alumina sludge waste-cement pastes containing $MnFe_2O_4$-nanoparticles. *Discover Applied Sciences, 6*, 567. https://doi.org/10.1007/s42452-024-06245-x

Ferone, C., Capasso, I., Bonati, A., Roviello, G., Montagnaro, F., Santoro, L., Turco, R., & Cioffi, R. (2019). Sustainable management of water potabilization sludge by means of geopolymers production. *Journal of Cleaner Production, 229*, 1–9. https://doi.org/10.1016/j.jclepro.2019.04.299

Gharieb, M., Ramadan, W., & Abd El-Gawad, W. M. (2023). Outstanding effect of cost-saving heavy nano-ferrites on the physico-mechanical properties, morphology, and gamma radiation shielding of hardened cement pastes. *Construction and Building Materials, 409*, Article 134064. https://doi.org/10.1016/j.conbuildmat.2023.134064

Hafez, A. I., Ali, H. M., Sabry, R. M., El-Masry, H. M., Walaa, M., & El-Gawad, A. (2023). Generation of novel, hygienic, inhibitive, and cost-effective nano-structured Core-shell pigments. *Progress in Organic Coatings, 175*, Article 107325. https://doi.org/10.1016/j.porgcoat.2022.107325

Hamed, E., & Demiröz, A. (2024). Optimization of geotechnical characteristics of clayey soils using fly ash and granulated blast furnace slag-based geopolymer. *Construction and Building Materials, 441*, Article 137488. https://doi.org/10.1016/j.conbuildmat.2024.137488

Hardjito, D., Wallah, S. E., Sumajouw, D. M. J., & Rangan, B. V. (2004). Factors influencing the compressive strength of fly ash-based geopolymer concrete. *Civil Engineering Dimension, 6*(2), 88–93.

He, Z., Wang, B., Shi, J., Rong, H., Tao, H., Jamal, A. S., & Han, X. (2024). Recycling drinking water treatment sludge in construction and building materials: A review. *Science of the Total Environment, 926*, Article 171513. https://doi.org/10.1016/j.scitotenv.2024.171513

Heikal, M., Ali, A. I., Ibrahim, B., & Toghan, A. (2020b). Electrochemical and physico-mechanical characterizations of fly ash-composite cement. *Construction and Building Materials, 243*, Article 118309. https://doi.org/10.1016/j.conbuildmat.2020.1183090

Heikal, M., Zaki, M. E. A., & Ibrahim, S. M. (2020a). Preparation, physico-mechanical characteristics and durability of eco-alkali-activated binder from blast-furnace slag, cement kiln-by-pass dust and microsilica ternary system. *Construction and Building Materials, 260*, Article 119947. https://doi.org/10.1016/j.conbuildmat.2020.119947

Ibrahim, S. M., Heikal, M., Abdelwahab, N. R., & Mohamed, O. A. (2023a). Fabricated CeO_2/ZrO_2 nanocomposite to improve thermal resistance, mechanical characteristics, microstructure and gamma radiation shielding of OPC composite cement pastes. *Construction and Building Materials, 392*, Article 131971. https://doi.org/10.1016/j.conbuildmat.2023.131971

Ibrahim, S. M., Heikal, M., & Mohamed, O. A. (2023b). Performance of CeO_2-nanoparticles on the mechanical and photocatalytic properties of composite cement. *Journal of Building Engineering, 68*, Article 106162. https://doi.org/10.1016/j.jobe.2023.106162

Jia, X., Zhou, Y., Zheng, J., Li, Y., Zou, H., & Xie, R. (2016). Cerium doped barium tantalates: Fabrication, characterization, and investigation of gamma radiation attenuation. *Journal of Alloys and Compounds, 688*, 679–684. https://doi.org/10.1016/j.jallcom.2016.07.188

John, S. K., Nadir, Y., & Girija, K. (2021). Effect of source materials, additives on the mechanical properties and durability of fly ash and fly ash-slag geopolymer mortar: A review. *Construction and Building Materials, 280*(19), Article 122443. https://doi.org/10.1016/j.conbuildmat.2021.122443

Khater, H. M., & Gharieb, M. (2024). Enhancing physico-mechanical properties and thermal stability of geopolymer composites through nano-material incorporation. *Discover Applied Sciences, 6*, 206. https://doi.org/10.1007/s42452-024-05863-9

Khoshkbijari, R. K., Farahmandfar, A., Zehni, N. Z., & Samimi, M. F. (2024). Properties of ground granulated blast-furnace slag-based geopolymer mortars containing glass powder, feldspar, and metakaolin under different curing conditions. *Construction and Building Materials, 435*, Article 136753. https://doi.org/10.1016/j.conbuildmat.2024.136753

Li, W., Chen, Z., Qin, G., Lian, S., Yao, G., Lin, J., Luo, S., & Huang, P. (2024). Equivalent thickness method of CFRP in chloride ion diffusion equation for CFRP–strengthened RC members and its load capacity assessment method. *Journal of Building Engineering, 98*, Article 111283. https://doi.org/10.1016/j.jobe.2024.111283

Liu, G., Li, J., & Zhang, Y. (2024). Corrosion of carbon steels subjected to chloride and sulfate in simulated concrete pore solutions with different pH. *Construction and Building Materials, 440*, Article 137445. https://doi.org/10.1016/j.conbuildmat.2024.137445

Luo, S., Li, W., Chen, Z., Guo, X., Li, D., Lin, J., Qin, G., & Huang, P. (2024). A simplified fatigue model for CFRP-strengthened RC beams under the coupling action of a hot–wet/saline environment and cyclic loading. *International Journal of Fatigue, 187*, Article 108444. https://doi.org/10.1016/j.ijfatigue.2024.108444

Maruthapandian, V., Muralidharan, S., & Saraswathy, V. (2016). Spinel NiFe2O4 based solid state embeddable reference electrode for corrosion monitoring of reinforced concrete structures. *Construction and Building Materials, 107*, 28–37. https://doi.org/10.1016/j.conbuildmat.2015.12.175

Mohamed, H., El-Gamal, A. A., Khalil, M. H., Hammed, H. H., & Rashad, A. M. (2022c). Valorization of nano-PbO as an additive to modify the properties and radiation shielding of alkali-activated slag mortar. *Materials Chemistry and Physics, 287*, Article 126277. https://doi.org/10.1016/j.matchemphys.2022.126277

Mohamed, O. A., El-dek, S. I., & El-Gamal, S. M. A. (2023a). Mechanical performance and thermal stability of hardened Portland cement-recycled sludge pastes containing $MnFe_2O_4$ nanoparticles. *Science and Reports, 13*, 2036. https://doi.org/10.1038/s41598-023-29093-y

Mohamed, O. A., El-Gamal, S. M. A., & Farghali, A. A. (2022a). Utilization of alum sludge waste for production of eco-friendly blended cement. *Journal of Material Cycles and Waste Management, 24*, 949–970. https://doi.org/10.1007/s10163-022-01369-x

Mohamed, O. A., Farghali, A. A., Eessaa, A. K., & El-Shamy, A. M. (2022b). Cost-effective and green additives of pozzolanic material derived from the waste of alum sludge for successful replacement of Portland cement. *Scientific Reports, 12*, 20974. https://doi.org/10.1038/s41598-022-25246-7

Mohamed, O. A., Hazem, M. M., Mohsen, A., & Ramadan, M. (2023b). Impact of microporous γ-Al_2O_3 on the thermal stability of pre-cast cementitious composite containing glass waste. *Construction and Building Materials, 378*, Article 131186. https://doi.org/10.1016/j.conbuildmat.2023.131186

Mohsen, A., Amin, M. S., Selim, F. A., & Ramadan, M. (2024). The impact of wurtzite and mesoporous Zn-Al-CO3 LDH on the performance of alkali-activated-slag: Setting times, compressive strength, and radiation attenuation. *Construction and Building Materials, 438*, Article 137218. https://doi.org/10.1016/j.conbuildmat.2024.137218

Niksarlıoğlu, S., Akman, F., Pekdemir, M. E., Kuzu, S. Y., Kaçal, M. R., & Yılmaz, M. (2023). An extensive investigation on gamma shielding properties of PLA/Gd_2O_3 nanocomposites. *Radiation Physics and Chemistry, 208*, Article 110936. https://doi.org/10.1016/j.radphyschem.2023.110936

Nonat, A. (2004). The structure and chemistry of the calcium silicate hydrates. *Cement and Concrete Research, 34*(9), 1521–1528. https://doi.org/10.1016/j.cemconres.2004.04.005

Owaid, H. M., Hamid, R., & Taha, M. R. (2019). Durability properties of multiple-blended binder concretes incorporating thermally activated alum sludge ash. *Construction and Building Materials, 200*, 591–603.

Pham, P. N., Duan, W., Zhuge, Y., Liu, Y., & Tormo, I. E. S. (2021). Properties of mortar incorporating untreated and treated drinking water treatment sludge. *Construction and Building Materials, 280*, Article 122558. https://doi.org/10.1016/j.conbuildmat.2021.122558

Ramadan, M., Amin, M. S., & Sayed, M. A. (2020). Superior physico-mechanical, fire resistivity, morphological characteristics and gamma radiation shielding of hardened OPC pastes incorporating ZnFe2O4 spinel nanoparticles. *Construction and Building Materials, 234*, Article 117807. https://doi.org/10.1016/j.conbuildmat.2019.117807

Ramadan, M., El-Gamal, S. M. A., Wetwet, M. M., & Hazem, M. M. (2024). Amelioration of antimicrobial, radiation shielding, thermal stability of Portland cement composites using hematite nanoparticles. *Construction and Building Materials, 421*, Article 135661. https://doi.org/10.1016/j.conbuildmat.2024.135661

Rashad, A. M., Eessaa, A. K., Khalil, M. H., & Mohamed, O. A. (2023). An initial study on the effect of nano-zirconium on the behavious of alkali-activated slag cement subjected to seawater attack. *Construction and Building Materials, 370*, Article 130659. https://doi.org/10.1016/j.conbuildmat.2023.130659

Reddy, B. C., Manjunatha, H. C., Vidya, Y. S., Sridhar, K. N., Pasha, U. M., Seenappa, L., Mahendra Kumar, C., Sadashivamurthy, B., Dhananjaya, N., Sathish, K. V., & Gupta, P. S. D. (2021). Radiation shielding, photoluminescence and antimicrobial properties of Magnesium ferrite synthesized via low temperature solution combustion method. *Progress in Nuclear Energy, 142*, Article 103988. https://doi.org/10.1016/j.pnucene.2021.103988

Richardson, I. G. (2008). The calcium silicate hydrates. *Cement and Concrete Research, 38*(2), 137–158. https://doi.org/10.1016/j.cemconres.2007.11.005

Sallam, O. I., Madbouly, A. M., Elalaily, N. A., & Ezz-Eldin, F. M. (2020). Physical properties and radiation shielding parameters of bismuth borate glasses doped transition metals. *Journal of Alloys and Compounds, 843*, Article 156056. https://doi.org/10.1016/j.jallcom.2020.156056

Santosa, G. Z. B., Filhoa, J. A. M., Pinheirob, M., & Manzato, L. (2019). Synthesis of water treatment sludge ash-based geopolymers in an Amazonian context. *Journal of Environmental Management, 249*, Article 109328. https://doi.org/10.1016/j.jenvman.2019.109328

Sayed, D. G., El-Gamal, S. M. A., El-Hosiny, F. I., Hazem, M. M., & Ramadan, M. (2024). Promoting the performance of green slag-based geopolymer using eskolaite nanoparticles for bio-mechanical, thermal, and shielding applications. *Construction and Building Materials, 433*, Article 136706. https://doi.org/10.1016/j.conbuildmat.2024.136706

Selim, F. A., Amin, M. S., Ramadan, M., & Hazem, M. M. (2020). Effect of elevated temperature and cooling regimes on the compressive strength, microstructure and radiation attenuation of fly ash–cement composites modified with miscellaneous nanoparticles. *Construction and Building Materials, 258*, Article 119648. https://doi.org/10.1016/j.conbuildmat.2020.119648

Shamaki, M., Adu-Amankwah, S., & Black, L. (2021). Reuse of UK alum water treatment sludge in cement-based materials. *Construction and Building Materials, 275*, Article 122047. https://doi.org/10.1016/j.conbuildmat.2020.122047

Shehata, N., Mohamed, O. A., Sayed, E. T., Abdelkareem, M. A., & Olabi, A. G. (2022). Geopolymer concrete as green building materials: Recent applications, sustainable development and circular economy potentials. *Science of the Total Environment, 836*, Article 155577. https://doi.org/10.1016/j.scitotenv.2022.155577

Tantawy, M. A. (2015). Characterization and pozzolanic properties of calcined alum sludge. *Materials Research Bulletin, 61*, 415–421. https://doi.org/10.1016/j.materresbull.2014.10.042

Taylor, H. F. W. (1997). *Cement chemistry* (2nd ed.). Thomas Telford Publishing.

Tobbala, D. E. (2019). Effect of Nano-ferrite addition on mechanical properties and gamma ray attenuation coefficient of steel fiber reinforced heavy weight concrete. *Construction and Building Materials, 207*, 48–58. https://doi.org/10.1016/j.conbuildmat.2019.02.099

Tran, N. P., Wang, T., Nguyen, T. N., Jin, H., & Ngo, T. D. (2024). High-volume recycled glass cementitious and geopolymer composites incorporating graphene oxide. *Construction and Building Materials, 450*, Article 138476. https://doi.org/10.1016/j.conbuildmat.2024.138476

Yu, R., Spiesz, P., & Brouwers, H. J. H. (2015). Effect of nano-silica on the hydration and microstructure development of Ultra-High Performance Concrete (UHPC). *Cement and Concrete Composites, 56*, 25–34. https://doi.org/10.1016/j.cemconcomp.2014.11.002

Yuan, Y., Ge, Y., Yan, J., Peng, H., & Zhang, B. (2024). Synthesis of geopolymer using glass fiber powder from retired wind blades: A new attempt to recycle solid waste in wind power industries. *Journal of Building Engineering, 95*, Article 110130. https://doi.org/10.1016/j.jobe.2024.110130

Zhang, J., Sun, N., Huo, Z., & Chen, J. (2024). Understanding the synergistic geopolymerization mechanism of multiple solid wastes in ternary geopolymers. *Journal of Building Engineering, 95*, Article 110295. https://doi.org/10.1016/j.jobe.2024.110295

Zhao, J., Wang, S., Wang, Z., Wang, K., & Fu, C. (2023). Bond performance between FRP bars and geopolymer concrete after elevated temperature exposure. *Construction and Building Materials, 384*, Article 131476. https://doi.org/10.1016/j.conbuildmat.2023.131476

Publisher's Note

Ola Abdelaziz Mohamed is an Associate Professor of physical chemistry, department of environmental science and industrial development; faculty of postgraduate studies for advanced sciences (PSAS), Beni-Suef University, Egypt.

Ahmed Hassan is a Professor of Reinforced Concrete Structure, Beni-suef University and served as Dean of the Faculty of Engineering at Beni Suef University (2021-2025).

Nesreen Ragheb Abd Elwahab is a Physics Researcher at Nuclear & Radiological Research Center, Egyptian Atomic Energy Authority, Egypt.